Supplementary Information (SI) for Energy & Environmental Science.

Supporting Information

Title: Spontaneous Passivation of Selective Zn (101) Plating via Dangling Bond Saturation and Electrostatic Interaction Regulation for High-Utilization, Fast-Kinetics Zinc Anodes

Author list: Yuxuan Zhang,[a] Minyoung Kim,[a] Dong Hun Lee,[a] Fei Qin,[a] Han-Wook Song,[b] Chung Soo Kim,[c] Jeongmin Park,[c][d] Chohee Kim,[c][e] Fang Lian,[f] and Sunghwan Lee*[a]

[a] Y. Zhang, F. Qin, D. H. Lee, and Prof. S. Lee*
School of Engineering Technology
Purdue University
West Lafayette, IN 47907, United States
E-mail: sunghlee@purdue.edu
[b] H.-W. Song
Convergence Research Center for Meta-Touch
Korea Research Institute of Standards and Science (KRISS)
267 Gajeong-ro, Yuseong-gu, Daejeon, 34113, Republic of Korea
[c] C. S. Kim, J. Park, and C. Kim
Analysis and Standards Center
Korea Institute of Ceramic and Technology
Jinju, 52851, Republic of Korea
[d] J. Park
Graduate School of Semiconductor Materials and Devices Engineering
Ulsan National Institute of Science and Technology
Ulsan, 44919, Republic of Korea
[e] C. Kim
Department of Materials Science and Engineering
Pusan National University
Pusan, 43241, Republic of Korea
[f] F. Lian
School of Materials Science and Engineering
University of Science and Technology Beijing
Beijing, 100083, PR China

Table of Contents

Experimental Section

Preparation of non-stoichiometric Sn-O compounds on Zn foil, Ultrathin (UT) Zn, and Cu foil. The $SnO_{1.17}$ and $SnO_{1.92}$ on the anodes (Zn foil, UT Zn, and Cu foil) were fabricated using a magnetron sputtering system for which a metal Sn target (99.999%, Kurt J. Lesker) was employed with O2 as the reactive sputter gas. The Zn metal foils were attached to a Si wafer substrate and were transferred to the sputter chamber from a load-lock chamber. The sputter chamber was further pumped down toward a base pressure under $2x10^{-7}$ Torr. During the depositions, the substrate was rotated at 5 rpm to ensure a uniform and homogeneous deposition. The atomic ratio of the non-stoichiometric Sn-O compounds was tuned by varying oxygen volume potential in the sputter gas (O_2/Ar): 13.5/86.5 and 16.5/83.5 for $SnO_{1.17}$ and $SnO_{1.92}$ respectively. The deposited samples were then annealed at 400 °C. The UT Zn foil anode was manufactured through a thermal evaporation system equipped with a 6 MHz oscillating quartz crystal sensor to monitor the growth rate and thickness.

Preparation of PEDOT@S electrode. The sulfur composites, carbon additives, and isopropyl alcohol were mixed by using a magnetic stirring bar to create a homogeneous slurry. The slurry was coated by a lab-scale blade on a battery-grade Ti foil and dried at room temperature in a fume hood. The dried electrode was attached to the substrate and transferred to the chamber of the oxidative chemical vapor deposition (oCVD) system. 3,4-Ethylenedioxythiophene (EDOT, 97%, Sigma Aldrich) and iron chloride ($FeCl_3$, 97%, Sigma Aldrich) were employed as the monomer and the oxidant to generate PEDOT polymer on the electrode (i.e., PEDOT@S electrode). After deposition, the electrode was rinsed with methanol to remove residuals and then dried in a fume hood. The mass loading of PEDOT@S is controlled at around 6 mg cm^{-2}. More detailed information on assembling PEDOT@S electrodes has been elaborated on in our previous papers.[1]

Preparation of MnO_2 powders. The MnO_2 powders were synthesized through a hydrothermal reaction. Manganese nitrate tetrahydrate ($Mn(NO_3)_2{\cdot}4H_2O$, 97%, Sigma Aldrich) was dissolved in a flask and prepared into $Mn(NO_3)_2$ solution with a concentration of 0.6 mol L^{-1}. Potassium permanganate ($KMnO_4$, 99.8%, Sigma Aldrich) was configured into a solution of 0.1 mol L^{-1}. Then 20 mL of $Mn(NO_3)_2$ solution and 20 mL of $KMnO_4$ solution were added into a Teflon-lined autoclave and heated at 140 °C for 12 h. The obtained product was collected, washed, and dried in a vacuum oven overnight.

Preparation of $ZnMn_2O_4$ powders. Zinc nitrate hexahydrate ($Zn(NO_3)_2$, 98%, Sigma Aldrich) and Manganese nitrate tetrahydrate ($Mn(NO_3)_2{\cdot}4H_2O$, 97%, Sigma Aldrich) were prepared into solution with a concentration of 0.2 mol L^{-1}. Then 15 mL of $Zn(NO_3)_2$ solution, 30 mL of $Mn(NO_3)_2$, and 480 mg carbon nanotubes were loaded in a flask with 27 mL ammonia solution ($NH_3{\cdot}H_2O$, 25%, Sigma Aldrich) as the additive. The uniformly mixed solution was heated at 180 °C for 3 h for evaporation. The obtained precipitation was centrifuged, washed with DI water and absolute ethanol, and dried at 70 °C in a vacuum oven overnight.

Preparation of MnO_2 and $ZnMn_2O_4$ electrode. MnO_2 powders or $ZnMn_2O_4$ powders were mixed with carbon additives and polyvinylidene difluoride (PVDF) in a mass ratio of 8:1:1. Specifically, the carbon additives were prepared by mixing carbon nanotubes and carbon black with a mass ratio of 9:1. PVDF was dissolved into a solution with a concentration of 6% by using the N-methyl−2-pyrrolidine (NMP) as the solvent. The obtained slurry was coated onto a Ti foil and then dried at 80 °C for 2 h. The mass loading of the obtained MnO_2 electrode and $ZnMn_2O_4$ electrode are controlled at around 6.5 mg cm^{-2} and 2.2 mg cm^{-2}, respectively.

Morphology and chemo-physical characterization. X-ray diffraction (XRD) patterns were obtained on a Panalytical Empyrean Powder X-ray diffractometer with the Cu Kα radiation at a scanning rate of 5° min^{-1}. Scanning electron microscopy (SEM) images were obtained on FEI Nova NanoSEM. Transmission electron microscopy (TEM) and high-resolution transmission electron microscopy (HRTEM) measurements were taken on an FEI Themis Z microscope. X-ray photoelectron spectroscopy (XPS) was carried out on a Thermo Fisher Scientific NEXSA. Contact angle measurement was performed on the Ramé-Hart goniometer (Model 590) optical contact angle system. The in-situ observation of Zn plating on

$SnO_{1.17}$@Zn, $SnO_{1.92}$@Zn, and Zn foil in the electrolyte of $ZnSO_4$ (2 mol L^{-1}) was performed by a digital camera integrated AmScope PZ620 optical microscope. 3D reconstruction images were obtained on a Leica DCM8 confocal microscope.

Electrochemical characterization. Linear scan voltammetry (LSV), cyclic voltammetry, Tafel plots, and electrochemical impedance spectroscopy (EIS with a frequency range from 100 mHz to 100 kHz) were performed on an electrochemical workstation (VersaSTAT3, Princeton). LSV and Tafel plots were obtained from a typical three-electrode system in a 2 mol L^{-1} Na_2SO_4 solution serving as electrolyte, where pristine Zn or $SnO_{1.17}$/$SnO_{1.92}$@Zn functions as the working electrode, Pt foil acts as the counter electrode, and Ag/AgCl serves as the reference electrode. The differential capacitance-potential measurements were conducted using an alternating current (AC) voltammetry test. The test parameters included a frequency of 6 Hz and an amplitude of 20 mV, with a scan rate of 10 mV s^{-1}. The potential range for these measurements extended from 0.9 to 0.3 V (vs. Zn^{2+}/Zn). The stability of Zn^{2+} plating/stripping was measured by symmetric Zn||Zn cells with the ZnSO4 solution of 2 mol L^{-1} as the electrolyte. The thickness of Zn foil and UT Zn foil is ~40 μm and ~2.8 μm respectively. Zn||Cu half-cells were utilized with a cut-off of 0.5 V to quantify the Coulombic efficiency (CE) and evaluate the feasibility of the anode-free system. In Zn||Cu half cells, a certain amount of Zn (0.5 mA cm^{-2} for 10 h) was plated on the Cu electrode, and charged to 0.5 V. The CE was calculated by the amount of zinc that can be stripped out in each cycle divided by the amount of plated (5 mAh cm^{-2}). Zn||S full cells were assembled by using PEDOT@S as the cathode and various Zn foils as the anode, with 120 μL of 1 mol L^{-1} $Zn(CH_3COO)_2$ solution with 0.05 wt % I_2 additive serving as the electrolyte. Zn||MnO_2 anode-less full cells were assembled by using the MnO_2 electrode paired with different UT Zn anodes, utilizing 100 μL of 2 mol L^{-1} $ZnSO_4$ solution as the electrolyte. 1.69 mg of $MnSO_4$ was added as the electrolyte additive. Additionally, Cu||$ZnMn_2O_4$ anode-free full cells were assembled by using $SnO_{1.17}$@Cu, $SnO_{1.92}$@Cu, and Cu foils as anodes paired with $ZnMn_2O_4$ cathodes in different configurations with 100 μL electrolyte (2 mol L^{-1} $ZnSO_4$ solution). The performances of Zn||Zn symmetric cells, Zn||Cu asymmetric cells, and full cells (i.e., Zn||S, Zn||MnO_2, and Zn||$ZnMn_2O_4$) were conducted at room temperature and collected by the Neware BTS-4000 battery test system. The electrochemical performances of half and full cells were evaluated in CR-2023 coin-type cells with glass microfiber filters (Whatman, GF/D) used as the separator.

Computational details. DFT calculations were carried out using the Quantum ESPRESSO.[2] The projector augmented wave (PAW) pseudopotentials are utilized to describe the core and valence electrons. The generalized gradient approximation based on the Perdew-Burke-Ernzerhof was employed to describe the electron exchange and correlation.[3] Amorphous structures of SnO1.92 were generated from the SnO2 crystal structure. Starting with this configuration, ab initio molecular dynamics (AIMD) simulations were performed for a temperature range from 1500 to 3000 K, which was above the melting point (2,966 K) of SnO2, to rapidly determine the equilibrium state. These generated structures were quenched to 0 K to obtain the total energies after AIMD simulation. The energy cut-off of 450 eV and the Monkhorst-Pack k-mesh of 2 × 2 × 1 were used to indicate the Brillouin zones of crystals with and without the adsorption of Zn2+. The adsorption energy (Eads) was calculated from the energy differences between the adsorbed Zn2+ on the substrate surface (Etotal) and the sum of the energy of the substrate crystal (Esub) and energy of the Zn2+ (EZn), which is defined as Eads= Etotal-(Esub+EZn). A vacuum layer of about 15 Å was applied to avoid the interaction between adjacent slabs. The energy barriers of Zn2+ transporting on different facets of Zn and Sn-O compounds were calculated by using the Nudge Elastic Band (CI-NEB) method. In all the calculations, the criterion for the electronic self-consistent field (SCF) loop was set to 1.0 × 10−5 eV atom-1. The atomic structures were optimized until the residual forces were below 0.05 eV $Å^{-1}$. FEA was performed by using COMSOL Multiphysics software to simulate the ion concentration distribution and electric field distribution in the cells with different Zn anodes. The transfer of ions is driven by migration because of the electric field and diffusion because of the concentration gradient which is governed by the Nernst−Planck equation:

$$N_i = -D_i(\nabla c_{0,i} - \frac{z_i F c_{0,i}}{RT}\nabla \Phi)$$

Where N_i is flux, D_i, z_i and $c_{0,i}$ is the diffusion coefficient, charge and concentration of species *i*, respectively. *F* is the Faraday's constant, *R* is the ideal gas constant, *T* is the Kelvin temperature and Φ is the electrolyte potential. Meanwhile, the ions in the electrolyte follow the equation of conservation of mass and charge:

$$\frac{\partial c_i}{\partial t} + \nabla \times N_i = 0$$

$$\sum_i z_i \, c_i = 0$$

where c_i is the concentration, z_i is the valence of each species in the electrolyte.

Basically, Zn2+ are transported from the bulk solution to the anode surface then reduced to Zn-atom, and at the interface of the electrolyte and the anode, the deposition process of Zn-ion can be described as the simplified reaction:

$$Zn^{2+} + 2e^{-} \leftrightarrow Zn$$

The electrochemical behaviors of Zn^{2+} at the electrode-electrolyte interface could be described by the famous Butler-Volmer equation:

$$i_{loc} = i_{ex}\left[\exp\left(\frac{\alpha_a F\eta}{RT}\right) - \exp\left(\frac{-\alpha_c F\eta}{RT}\right)\right]$$

where i_{loc} is the local current density, which could be used to quantify the local reaction rate. η is overpotential, α_a and α_c are the anodic and cathodic charge transfer coefficients, respectively, and i_{ex} is exchange current density. The overpotential can be calculated as:

$$\eta = \phi_s - \phi_e - U_{eq}$$

where ϕ_s and ϕ_l is the solid phase and liquid phase potential, respectively, U_{eq} is the equilibrium potential of the reaction.Therefore, boundary conditions near the anode substrate can be described as:

$$N_{Zn^{2+}} \cdot \boldsymbol{n} = -\frac{i_0}{2F}[\exp\left(\frac{\alpha_a F\eta}{RT}\right) - \frac{c_{zn^{2+}}}{c_0}\exp\left(\frac{\alpha_c F\eta}{RT}\right)]$$

where ***n*** is the normal vector of the boundary. Schottky contact and Ohmic contact were constructed at the bottom of the side of the Sn-O compound layer in $SnO_{1.17}$@Zn and $SnO_{1.92}$@Zn models, respectively. In the simplified 2D model cell, the electrolyte region was set as a square with a width of 5 μm. The length and width of electrodes on the top and bottom of the electrolyte were designed to be 0.25 and 5 μm, respectively. The humps (0.4 μm in height, 0.3 μm in width) were used to represent the initial Zn grains. The rectangle region in the electrolyte (0.05 μm in height and 5 μm in width) was set to indicate the Sn-O compounds layer. The anode (the lower boundary of the model) was set as the ground (0 V). The initial concentration of the Zn^{2+} cation and SO_4^{2-} anion was set to 2 mol L^{-1}.

Variable name	Symbol	Value
Diffusivity of Zinc ion	D_i	*3.68×10-10 m2 s-1*
Conductivity of electrolyte	*σe*	*107 S m-1*
Conductivity of electrolyte	*σs*	*4.64 S m-1*
Site density of the electrolyte	*c0*	*5.625×104 mol m-3*
Site density of electrode	*cs*	*1.092×105 mol m-3*
Transfer coefficient	*α*	*0.5*
Electron Transfer	*n*	*2*
Kinetic coefficient	*Lη*	*0.001 s-1*
Band gap	*Eg0*	*0.7 eV and 3.6 eV*
Electron affinity	*chi0*	*5.4 eV and 4.5 eV*
Work function of metal	*Wf*	*4.3 eV*

Table S1. Materials parameters used in FEA simulations.

Supplementary Notes

Supplementary Note 1 | Theoretically required thickness of metallic Zn

The calculation was performed assuming an N/P ratio of 1.08 and a cathode areal capacity of $4\ mAh\ cm^{-2}$ for the Zn metal battery, based on the parameters of a commercialized Li-ion battery. The theoretical density (ρ) and specific capacity (S_C) of metallic Zn are $7.14\ g\ cm^{-3}$ and $820\ mAh\ g^{-1}$ respectively. To provide an anode areal capacity of $4.32\ mAh\ cm^{-2}$ ($4\ mAh\ cm^{-2} \times 1.08$), the mass loading ($m$) of the metallic Zn was calculated using the formula $m = \frac{4.32\ mAh\ cm^{-2}}{S_c} = 5.26 \times 10^{-3}\ g\ cm^{-2}$. The thickness ($t$) of the required metallic Zn is calculated as $t = \frac{m}{\rho} = 7.4\ \mu m$. Thus, the theoretical thickness of the metallic Zn for a Zn metal battery with a cathode areal capacity of $4\ mAh\ cm^{-2}$ and an N/P ratio of 1.08 is approximately $7.4\ \mu m$. Similarly, the theoretical thickness of metallic Zn of $20\ mAh\ cm^{-2}$ is calculated as $34\ \mu m$.

Supplementary Note 2 | Texture coefficient of crystal planes (Tc) of Zn

The orientations of plated Zn can be esitimated by calculating the texture coefficient (Tc) according to the equation:

$$T_C = \frac{I_{(hkl)}/I_{0(hkl)}}{\frac{1}{n}\sum(I_{(hkl)}/I_{0(hkl)})}$$

where $I_{(hkl)}$ is the peak intensity of plated Zn and the index 0 refers to the intensities for the standard Zn sample taken from a powder diffraction file card (PDF# 99-0110). n is the number of diffraction planes considered in the analysis.[4]

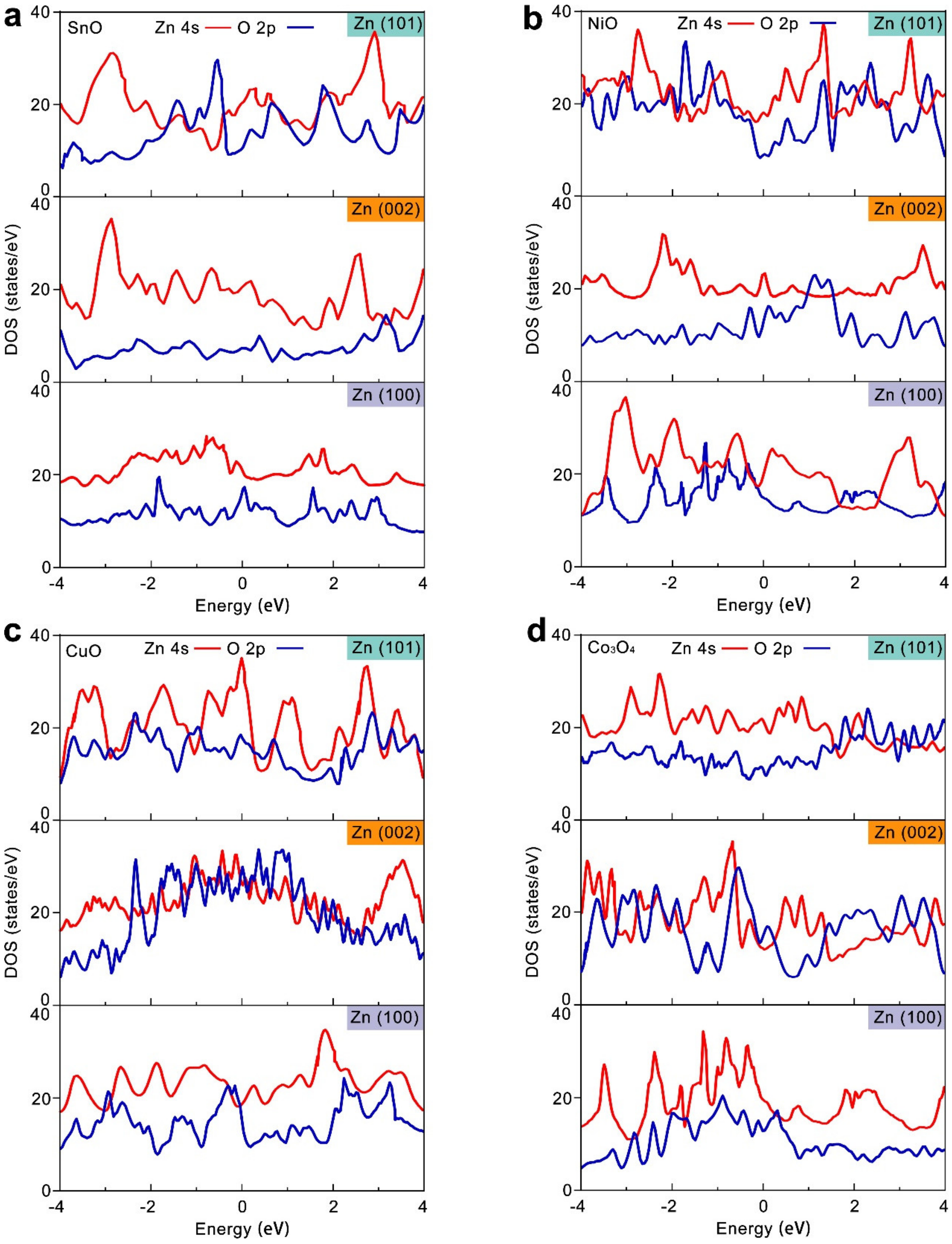

Figure S1. The pDOS of Zn 4s and O 2p orbitals of (a) SnO@Zn, (b) NiO@Zn, (c) CuO@Zn, and (d) Co_3O_4@Zn

The overlaps of electron orbital wavefunctions $\langle \psi_{\overline{n}} | \psi_n \rangle$ can be calculated within the projector augmented wave (PAW) formalism from the pseudo wave functions and their projector overlaps by the following equation[5]:

$$\langle \psi_{\overline{n}} | \psi_n \rangle = \langle \overline{\psi}_{\overline{n}} | \overline{\psi}_n \rangle + \sum_a \sum_{i_1 i_2} \langle \overline{\psi}_{\overline{n}} | \overline{p}^a_{i_1} \rangle \, \Delta S^a_{i_1 i_2} \, P^a_{n i_2}$$

where $\Delta S^{a}_{i_1 i_2} = \langle \phi^{a}_{i_1} | \phi^{a}_{i_2} \rangle - \langle \overline{\phi}^{a}_{i_1} | \overline{\phi}^{a}_{i_2} \rangle$ is the overlap metric, $\phi^{a}_{i_1}$, $\phi^{a}_{i_2}$, and $\overline{p}^{a}_{i_1}$ are the partial waves, pseudo partial waves, and projector functions.

	Zn 4s of Zn (101)	Zn 4s of Zn (002)	Zn 4s of Zn (100)
O 2p of SnO	1.43×10^{-6}	0.57×10^{-6}	0.44×10^{-6}
O 2p of NiO	1.26×10^{-6}	0.41×10^{-6}	0.89×10^{-6}
O 2p of CuO	0.64×10^{-6}	1.23×10^{-6}	0.51×10^{-6}
O 2p of Co_3O_4	0.85×10^{-6}	1.16×10^{-6}	0.62×10^{-6}

Table S2. Overlap factors of O 2p and Zn 4s

The projected density of states (pDOS) was calculated to investigate the effects of SnO, NiO, CuO, and Co_3O_4 on reducing surface energy. As shown in Figures S1a and Table S1, SnO exhibits higher overlap factors of 1.43×10^{-6} between the O 2p orbital and the Zn 4s orbital on the Zn (101) plane while displaying smaller overlap factors for both the Zn (002) and Zn (100) planes. This indicates that SnO interacts strongly and selectively with Zn (101), compared to other Zn orientations. In contrast, NiO in Figure S1b shows a non-selective bonding saturation behavior that displays strong overlap factors for multiple Zn facets of 1.26×10^{-6} for Zn (101) and 0.89×10^{-6} for (100). CuO and Co_3O_4 show strong pDOS overlap between the Zn 4s orbital on the Zn (002) plane and the O 2p orbital as indicated in Figure S1c and S1d, with only faint overlap observed for the Zn (101) and Zn (100) planes. This suggests that CuO and Co_3O_4 interact more weakly with Zn (101). Finally, between SnO and NiO, both of them effectively saturating Zn dangling bonds on the Zn (101) surface and consequently reducing the surface energy of the Zn (101) plane, the SnO that can selectively grow Zn (101) orientation was selected for further investigation in our study.

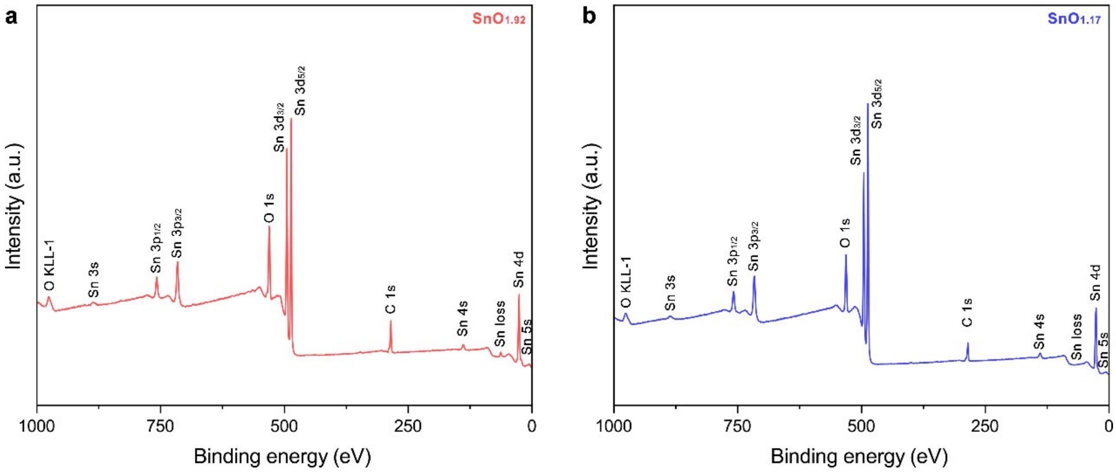

Figure S2. XPS survey scans of (a) $SnO_{1.92}$ and (b) $SnO_{1.17}$ interphases.

Figure S2 shows the XPS survey scans of (a) $SnO_{1.92}$ and (b) $SnO_{1.17}$, measured over a binding energy range of 0 to 1000 eV. XPS signals from Sn 3d and O 1s are detected in $SnO_{1.92}$ as illustrated in Figure S1a, along with additional Sn-related peaks from Sn 3s, 3p, 4s, and 4d excitations. Similarly, the prominent Sn 3d and O 1s signals are observed in $SnO_{1.17}$. To further analyze the bonding and chemical information of $SnO_{1.92}$ and $SnO_{1.17}$ interphases, high-resolution scans of Sn 3d and O 1s were performed.

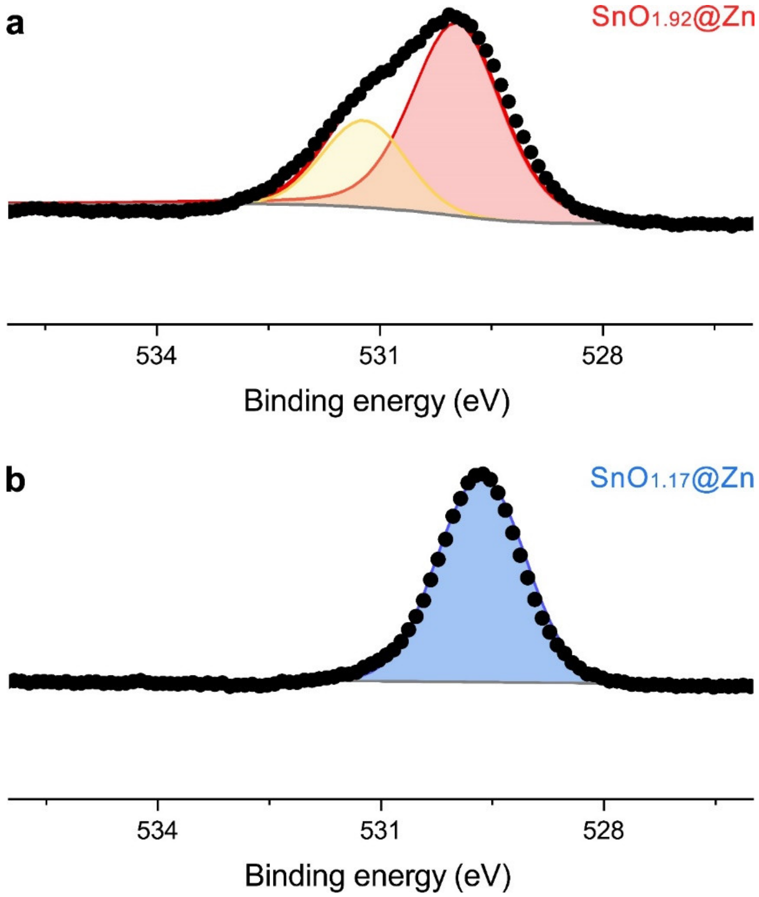

Figure S3. HR XPS spectra of O 1s based on (a) $SnO_{1.92}$ and (b) $SnO_{1.17}$ interphases.

In $SnO_{1.92}$@Zn, the high-resolution (HR) O 1s spectrum shows an asymmetric peak (Figure S3a), which is deconvoluted into two components: a strong peak at 529.8 eV, corresponding to lattice oxygens in SnO_2, and a weaker peak at 531.4 eV, associated with the presence of oxygen-related defects or the hydroxyl group. In contrast, the overall O 1s peak in $SnO_{1.17}$@Zn is shifted to a lower binding energy (Figure S3b), attributed to the non-stoichiometric SnO (i.e, $SnO_{1.17}$) interphase, indicating a lower valence state of O in $SnO_{1.17}$ compared to $SnO_{1.92}$.

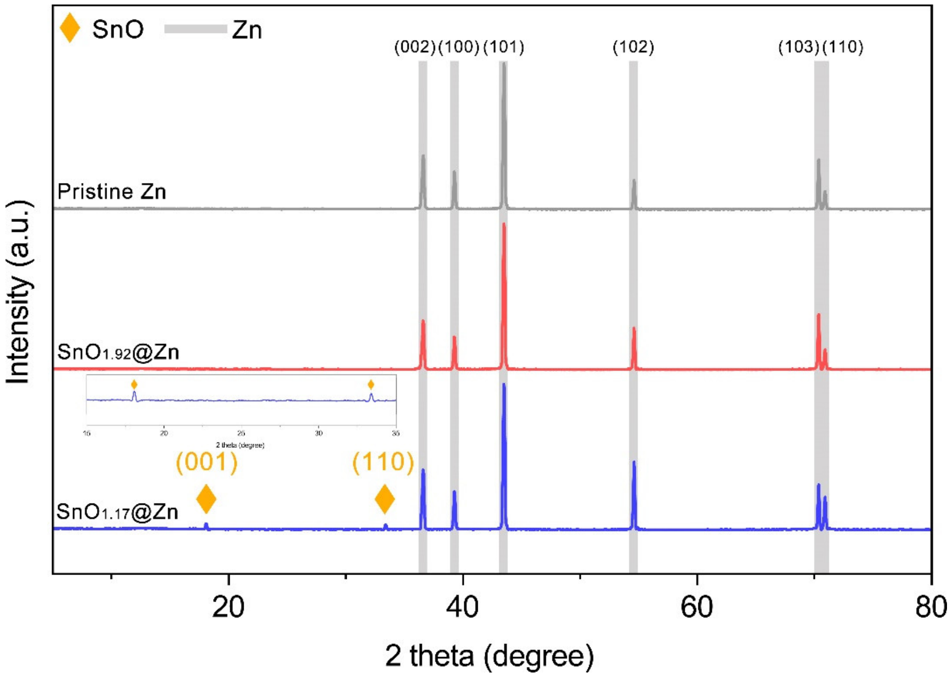

Figure S4. XRD patterns of as-fabricated pristine Zn, $SnO_{1.92}$@Zn, and $SnO_{1.17}$@Zn.

Distinguished peaks at 36.3°, 38.9°, 43.2°, 54.3°, 70.1°, and 70.6°, which are attributed to the metallic Zn, are observed in pristine Zn, $SnO_{1.92}$@Zn, and $SnO_{1.17}$@Zn. In addition, weak peaks located at 18.1° and 33.4° in $SnO_{1.17}$@Zn are attributed to polycrystalline SnO phases.

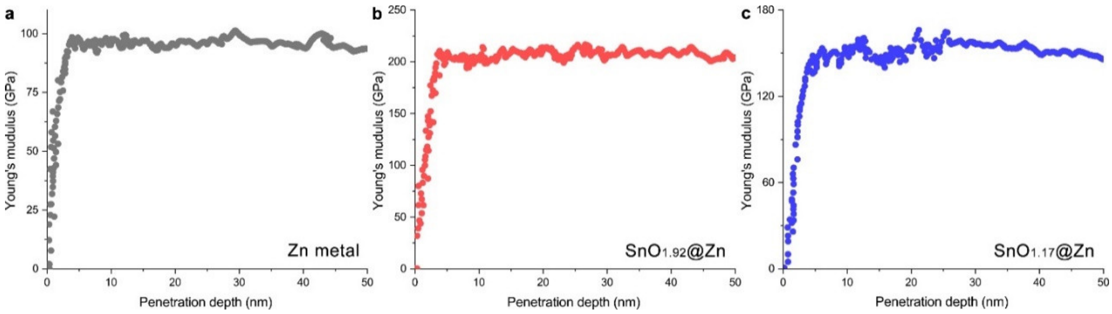

Figure S5. Young's modulus-displacement curve for (a) Zn metal, (b) $SnO_{1.92}$@Zn, and $SnO_{1.17}$@Zn.

Sample	**Elastic Deformation Energy Density (Ue)**
Pristine Zn	0.64 J cm^{-3}
$SnO_{1.17}$@Zn	1.87 J cm^{-3}
$SnO_{1.92}$@Zn	2.32 J cm^{-3}

Table S3. Elastic deformation energy density (Ue) of pristine Zn, $SnO_{1.17}$@Zn, and $SnO_{1.92}$@Zn.

Nanoindentation tests were performed to assess the dynamic mechanical properties of Zn metal, $SnO_{1.92}$@Zn, and $SnO_{1.17}$@Zn. The load-displacement curves of Zn metal, $SnO_{1.92}$@Zn, and $SnO_{1.17}$@Zn are presented in the insets of Figure S5, from which the corresponding Young's modulus values are derived. The Young's modulus-displacement curve indicates that Zn metal has a Young's modulus of approximately 95 GPa as shown in Figure S5a, consistent with reported values of ~100 GPa. The Young's modulus for $SnO_{1.92}$@Zn (Figure S5b) and $SnO_{1.17}$@Zn (Figure S5c) was determined to be ~207 GPa and ~152 GPa, respectively, significantly higher than that of Zn metal. In addition, the elastic deformation energy density (U_e) of pristine Zn, $SnO_{1.17}$@Zn, and $SnO_{1.92}$@Zn have been calculated through classical contact theories developed by Hertz and Sneddon,[6] which describes the mechanistic evolution of two linear elastic bodies (i.e., the probe of nanoindentation and the test sample) under infinitesimal deformation range. U_e represents the amount of potential energy stored per unit volume when a material undergoes elastic deformation. A higher U_e indicates that the interphase can withstand greater mechanical stress and sustain volume expansion without structural failure. As indicated in Table S3, $SnO_{1.17}$@Zn and $SnO_{1.92}$@Zn show Ue of 1.87 and 2.32 J cm^{-3}, which are higher than the 0.64 J cm^{-3} of the pristine Zn.

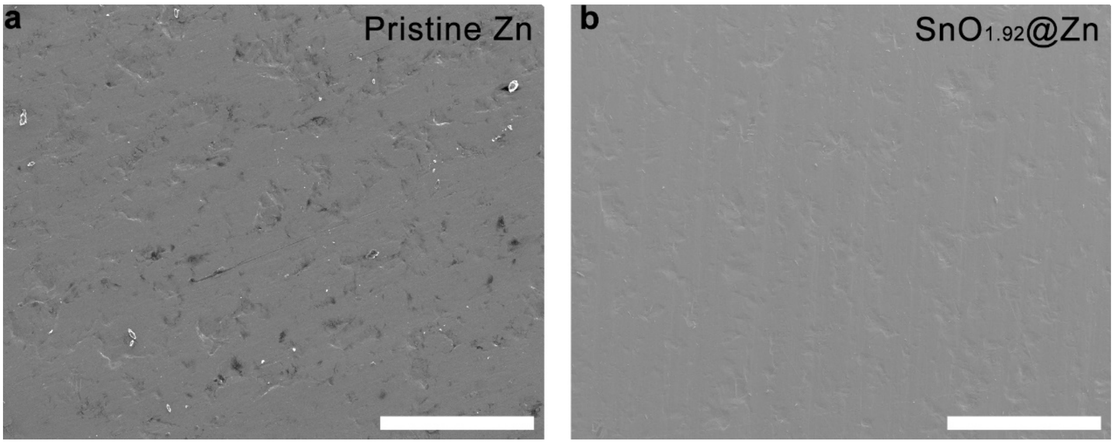

Figure S6. SEM images of as-fabricated (a) pristine Zn anode and (b) $SnO_{1.92}$@Zn (scale bar, 100 μm).

Similar to the smooth, flat surface of $SnO_{1.17}$@Zn shown in Figure 2e, $SnO_{1.92}$@Zn also exhibits a smooth, clean surface compared to the pristine Zn, indicating the uniform coating of both Sn-O interphases on the metallic Zn.

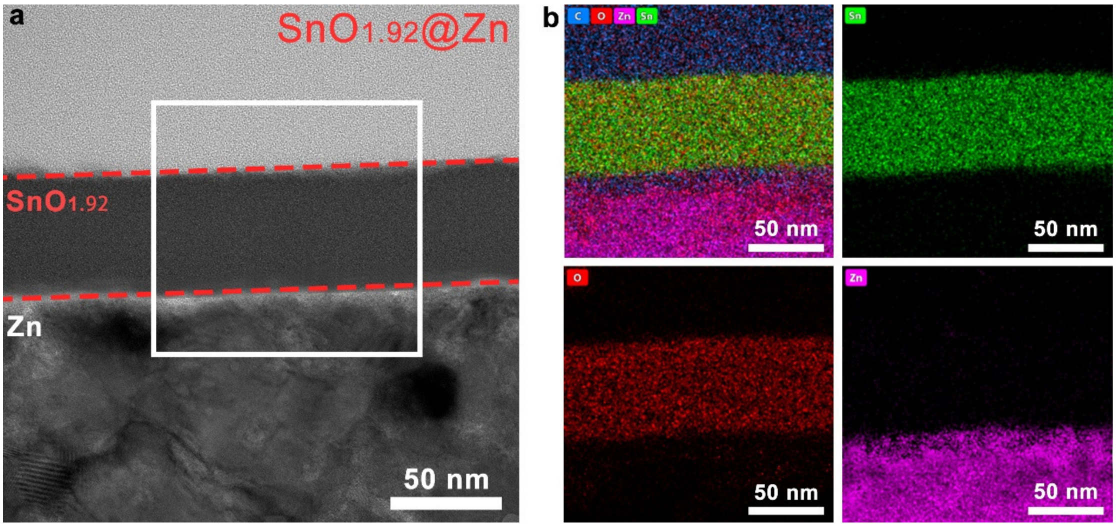

Figure S7. (a) TEM images, and (b) EDX mapping of $SnO_{1.92}$@Zn.

The cross-sectional TEM image and EDX mapping reveal that the $SnO_{1.92}$ interphase, with a thickness of approximately 65 nm, is uniformly coated on the Zn foil.

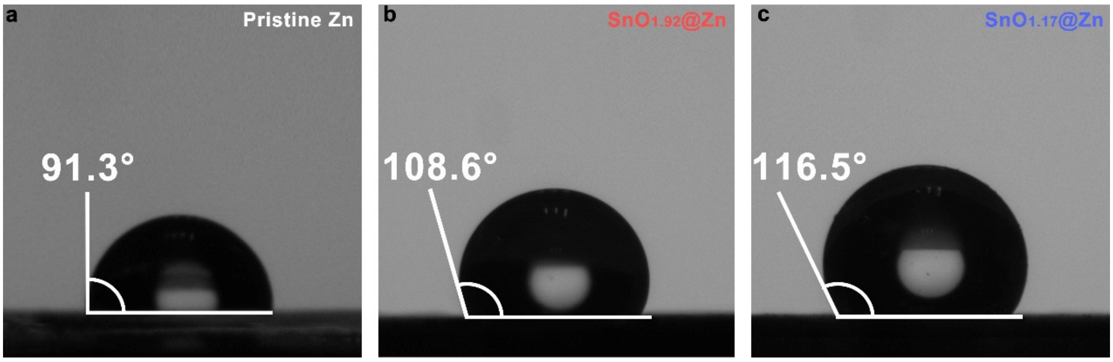

Figure S8. Contact angle measurements of 2 M $ZnSO_4$ aqueous electrolyte on the surface of (a) pristine Zn, (b) $SnO_{1.92}$@Zn, and (c) $SnO_{1.17}$@Zn.

The $SnO_{1.17}$ interphase exhibits stronger hydrophobicity, as evidenced by a larger contact angle of 116.5° for an aqueous electrolyte droplet on the $SnO_{1.17}$ surface, compared to 108.6° on $SnO_{1.92}$ and 91.3° on bare Zn. This enhanced hydrophobicity of the $SnO_{1.17}$ interphase helps isolate the active Zn, particularly (101) orientation in this study, from the bulk electrolyte, thereby inhibiting water-induced erosion.

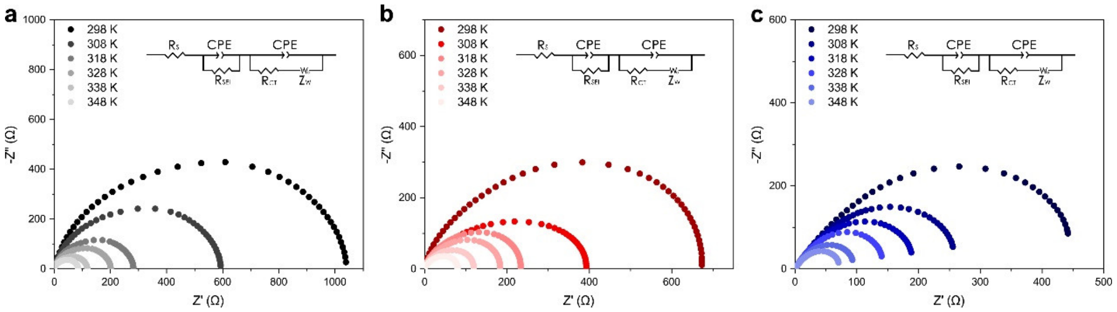

Figure S9. Nyquist plots (inset is the equivalent circuit model) of (a) Pristine Zn, (b) $SnO_{1.92}$@Zn, and (c) $SnO_{1.17}$@Zn-based symmetric cells at different temperatures.

The activation energy (E_a) for charge transfer resistance (R_{ct}) of different Zn electrodes can be measured by the Nyquist plots of symmetric Zn cells with temperature-dependent EIS measurements. Figure S8 displays the Nyquist plots of symmetric cells based on the pristine Zn, $SnO_{1.92}$@Zn, and $SnO_{1.17}$@Zn anodes at different temperatures. The activation energy for desolvation of hydrated Zn^{2+} is estimated according to the Arrhenius equation:

$$R_{ct} = A \times e^{-\frac{E_a}{RT}}$$

where Rct, A, Ea, R, and T are the charge-transfer resistance, Arrhenius constant, desolvated activation energy, gas constant, and absolute temperature, respectively. By linearly fitting ln(1/R_{ct}) versus 1000/T, the E_a for each anode can be obtained from the slope from the corresponding Arrhenius plots in Figure 3f. The calculated Ea of pristine Zn, $SnO_{1.92}$@Zn, and $SnO_{1.17}$@Zn anodes are 41.8, 35.7, and 30.6 KJ mol−1, respectively, of which the lowest Ea of the $SnO_{1.17}$@Zn anode indicates an optimized kinetic behavior for Zn^{2+} de-solvation and facilitating fast ion transport through the $SnO_{1.17}$ interface layer.

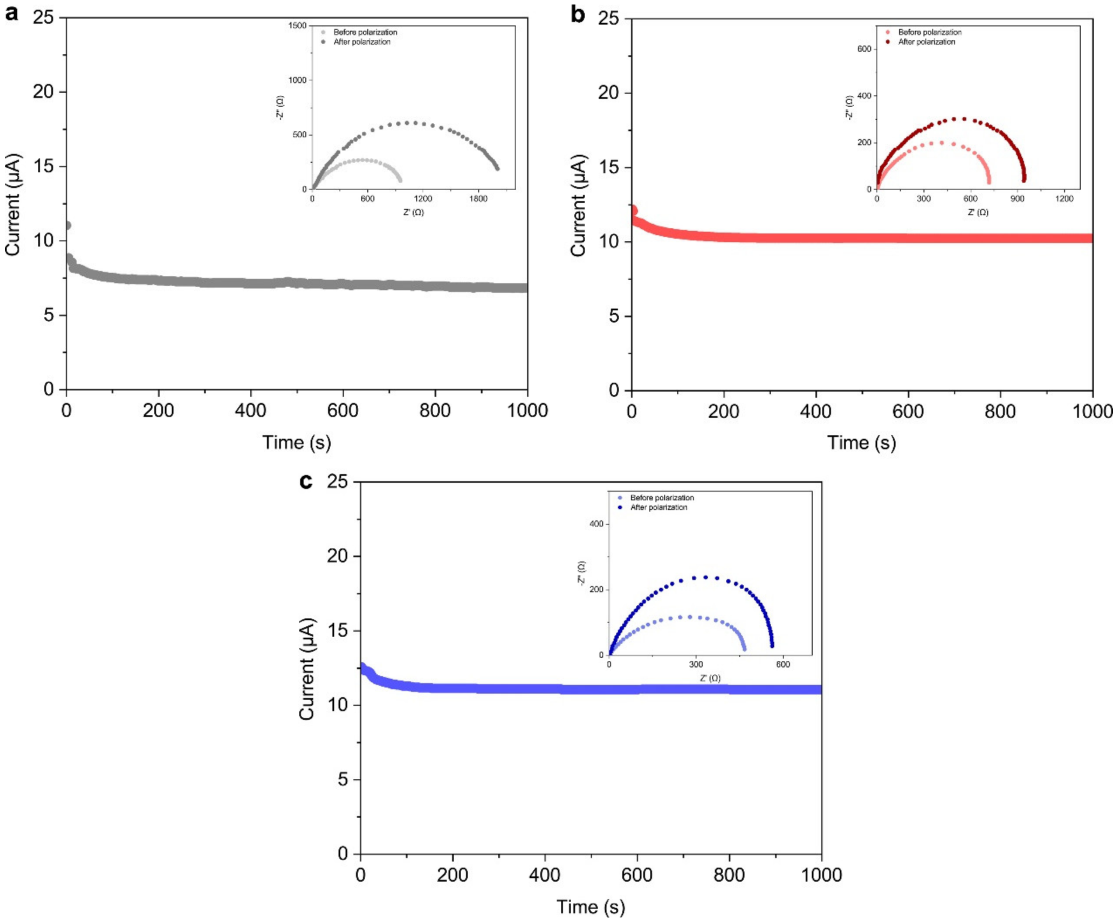

Figure S10. Current-time plots of (a) Pristine Zn, (b) $SnO_{1.92}$@Zn, and (c) $SnO_{1.17}$@Zn symmetric cells after polarization at a constant potential of 15 mV. The inset is the corresponding Nyquist plots of the cell before and after polarization.

The measurement of the Zn^{2+} transference number is estimated according to the typical Bruce-Vincent method described as the following equation[7]:

$$t_{Zn^{2+}} = \frac{I_S(\Delta V - I_0 R_0)}{I_0(\Delta V - I_S R_S)}$$

where ΔV is the constant polarization voltage applied (15 mV); I_0 is the initial current (11.06 μA for pristine Zn; 12.13 μA for $SnO_{1.92}$@Zn; 12.59 μA for $SnO_{1.17}$@Zn) and R_0 is the initial charge transfer resistance (~926 Ω for pristine Zn; ~643 Ω for $SnO_{1.92}$@Zn; ~452 Ω for $SnO_{1.17}$@Zn); and I_s is the steady-state current (6.89 μA for pristine Zn; 10.44 μA for $SnO_{1.92}$@Zn; 11.16 μA for $SnO_{1.17}$@Zn) and R_s is the steady-state charge transfer resistance (~1947 Ω for pristine Zn; ~954 Ω for $SnO_{1.92}$@Zn; ~525 Ω for $SnO_{1.17}$@Zn), respectively. The calculated $t_{Zn^{2+}}$ of pristine Zn, $SnO_{1.92}$@Zn, and $SnO_{1.17}$@Zn anodes are 0.41, 0.67, and 0.86, respectively, of which the highest $t_{Zn^{2+}}$ obtained from the $SnO_{1.17}$@Zn anode ensures the uniform Zn^{2+} plating.

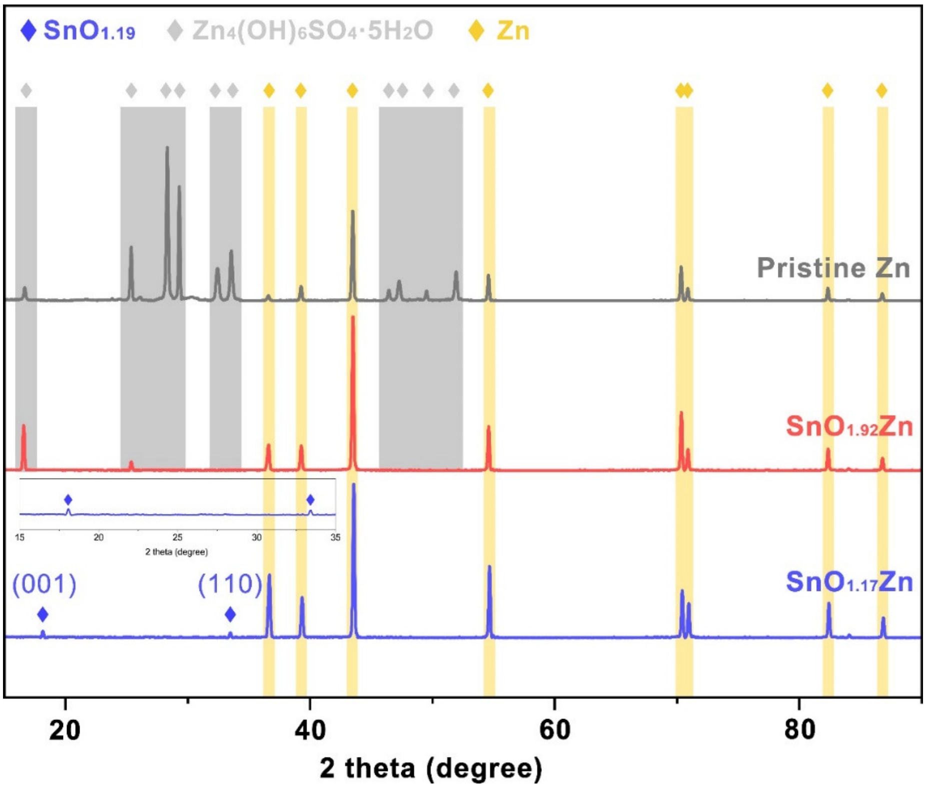

Figure S11. XRD results of pristine Zn, $SnO_{1.92}$@Zn, and $SnO_{1.17}$@Zn foils soaked in 2 M ZnSO4 electrolyte for 5 days.

After 5 days of soaking, strong XRD signals corresponding to the by-product $Zn_4SO_4(OH)_6 \cdot 5H_2O$ are detected on the pristine Zn in Figure S9. As is well known, the formation of $Zn_4SO_4(OH)_6 \cdot 5H_2O$ is induced by the hydrogen evolution reaction (HER) on Zn which increases the local pH near the Zn surface, leading to the precipitation reaction ($4Zn^{2+} + SO_4^{2-} + 6OH^- + 5H_2O \rightarrow Zn_4SO_4(OH)_6 \cdot 5H_2O$). $Zn_4SO_4(OH)_6 \cdot 5H_2O$ is also identified in $SnO_{1.92}$@Zn, with peaks around 16.7° and 25.8°, indicating a slight corrosion process. In contrast, no peaks corresponding to $Zn_4SO_4(OH)_6 \cdot 5H_2O$ are observed in $SnO_{1.17}$@Zn after soaking in 2 M ZnSO4 electrolyte for 5 days, indicating that the $SnO_{1.17}$ interphase effectively inhibited the corrosion process.

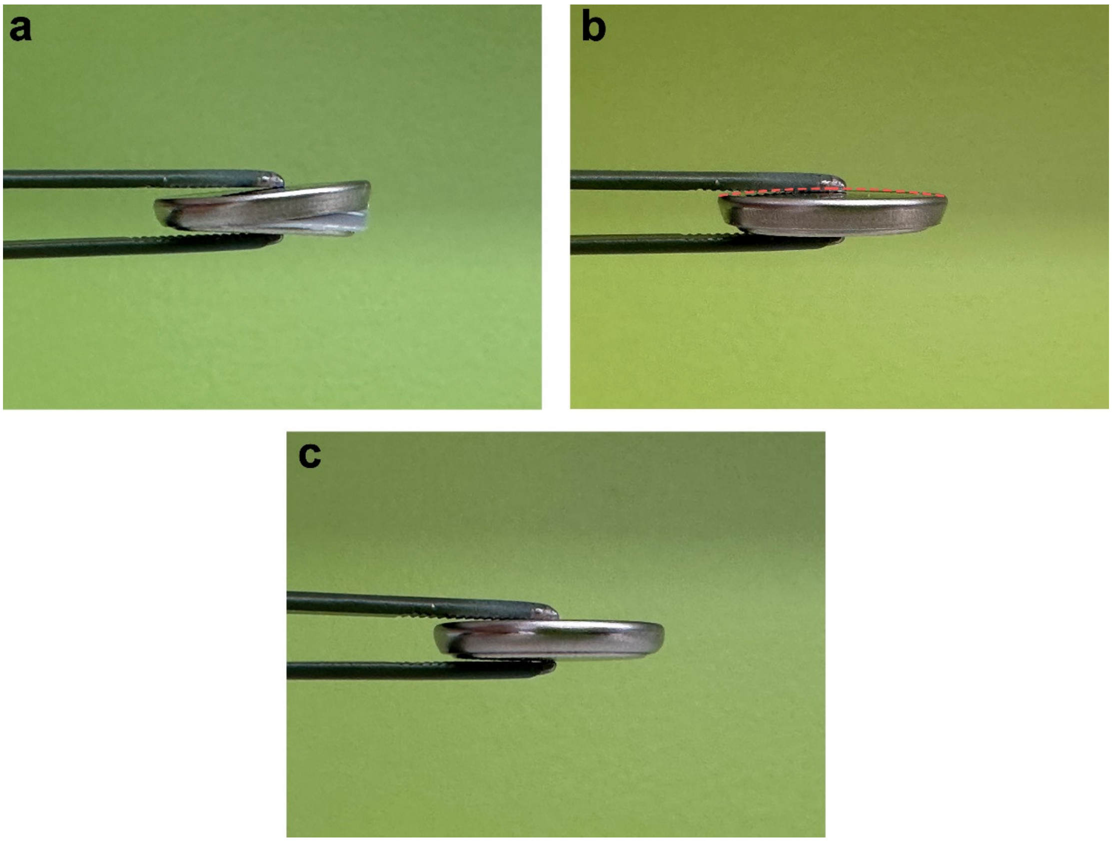

Figure S12. Optical images of symmetric cells with the three anodes after cycling. (a) Symmetric cell with pristine Zn anode. (b) Symmetric cell with $SnO_{1.92}$@Zn anode. (c) Symmetric cell with $SnO_{1.17}$@Zn anode.

The drastic hydrogen evolution reaction (HER) in the cell with the pristine Zn anode resulted in the accumulation of H_2 gas. The sealed coin cell was expanded and the top case and the bottom case were detached due to the high internal pressure as shown in Figure S11a. The top case of the cell with $SnO_{1.92}$@Zn anode shows a convex shape which was led by the increased internal pressure (Figure S11b) where the HER process in the cell with $SnO_{1.92}$@Zn anode is partially inhibited by the semiconductor coating layer. For the cell with $SnO_{1.17}$@Zn anode, there is no distinct shape variation that can be observed on the cell after cycling, which implies the HER process in the cell has been successfully restricted by the $SnO_{1.17}$ coating layer.

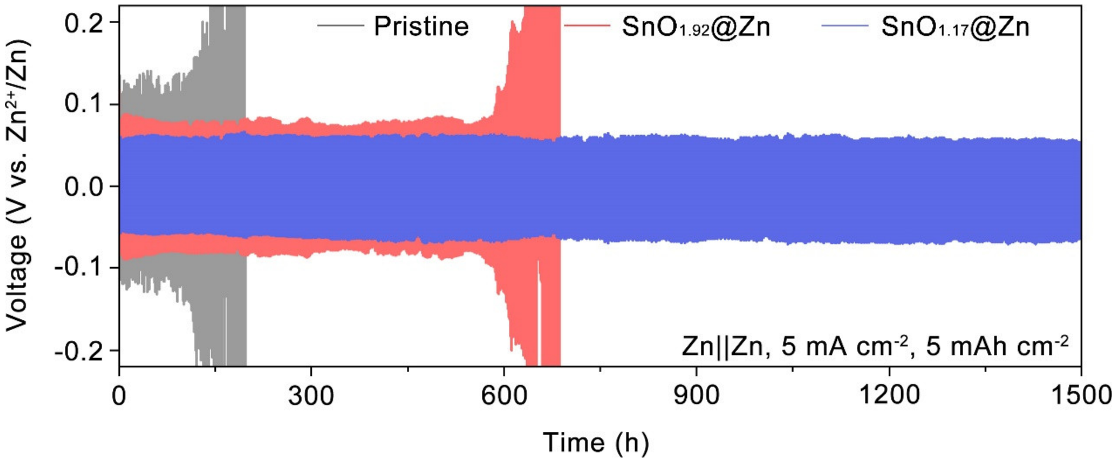

Figure S13. Galvanostatic cycling performances of the symmetric cells with Pristine Zn, $SnO_{1.92}$@Zn, and $SnO_{1.17}$@Zn electrodes at 5 mA cm^{-2}, 5 mAh cm^{-2}.

The cycling performances of symmetric cells with the pristine Zn, $SnO_{1.92}$@Zn, and $SnO_{1.17}$@Zn electrodes were tested under 5 mA cm-2. The symmetric cell with $SnO_{1.17}$@Zn electrode exhibited long cycling stability over 1500 h a 5 mAh cm−2, which is around 8-fold and 2-fold longer lifespan compared to the pristine Zn (~190 h) and $SnO_{1.92}$@Zn (~700 h) cells.

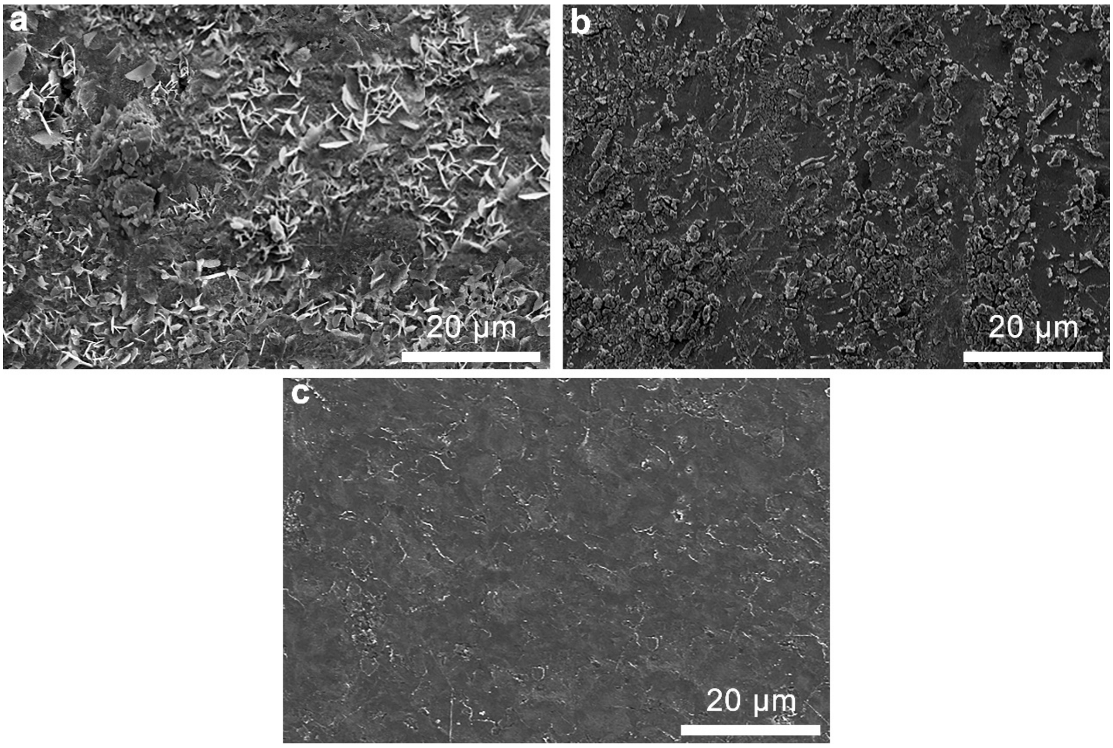

Figure S14. SEM images of various anodes in symmetric cells after cycling. (a) Pristine Zn anode, (b) $SnO_{1.92}$@Zn anode, and (c) $SnO_{1.17}$@Zn anode after cycling for 100 h at 5 mA cm^{-2} with 5 mAh cm^{-2}.

The SEM image of the pristine Zn anode after cycling for 100 h of cycling reveals a surface characterized by pronounced protrusions, extensive flake-like by-products, and micro-sized cavities, as illustrated in Figure S13a. These features indicate the unevenness of Zn^{2+} stripping-plating behavior and the severity of the HER process of pristine Zn anode. The surface of the $SnO_{1.92}$@Zn anode after 100 h of cycling shows significantly lower roughness compared to the pristine Zn anode. However, there are considerable accumulated by-products, with sub-micrometer dimensions, observable on the surface of the cycled anode (Figure S13b). In contrast, the surface of the $SnO_{1.17}$@Zn anode after cycling for 100 h maintains a compact and uniform surface without by-product formation, suggesting the strong resistance to the side reactions on HER and dendrite formation during the Zn^{2+} stripping/plating process.

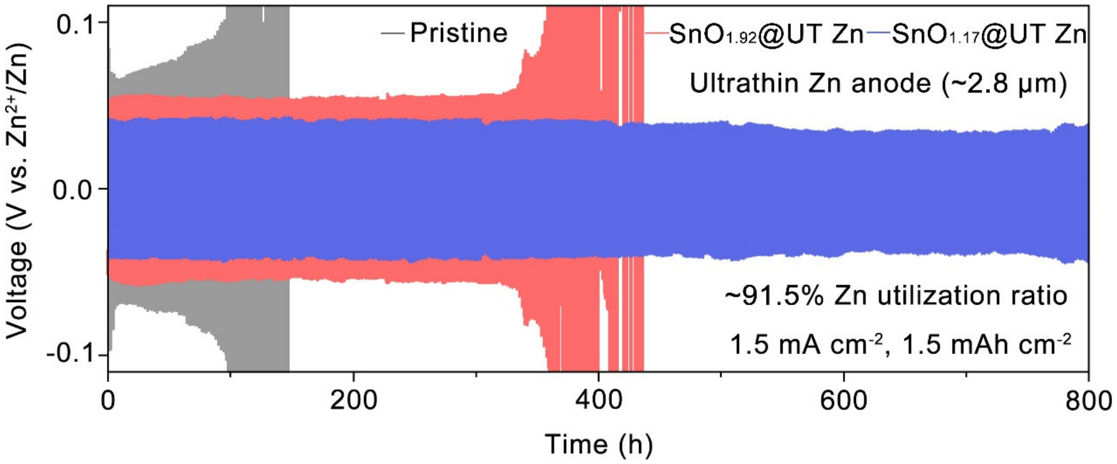

Figure S15. Galvanostatic cycling performances of pristine ultrathin (UT) Zn, $SnO_{1.92}$@UT Zn, and $SnO_{1.17}$@UT Zn symmetric cells at 1.5 mA cm^{-2} and 1.5 mAh cm^{-2} with a depth of discharge of 91.5%.

The stripping/plating performance of Zn^{2+} on the UT Zn anode was evaluated based on cells with the pristine UT Zn, $SnO_{1.92}$@UT Zn, and $SnO_{1.17}$@UT Zn electrodes.

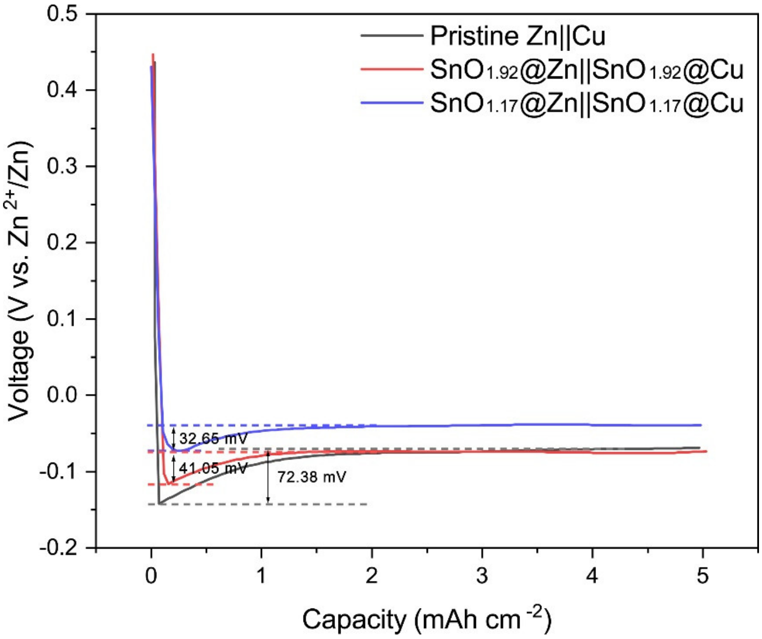

Figure S16. The first discharge profiles of Zn||Cu asymmetric cells at 10 mA cm^{-2} with a fixed capacity of 5 mAh cm^{-2}.

Figure S15 displays the voltage profiles of Zn electrodeposition upon various substrates including Cu, $SnO_{1.92}$@Cu, and $SnO_{1.17}$@Cu. On the $SnO_{1.17}$@Cu substrate, the lower nucleation overpotential of 32.65 mV is recorded, which is well below that of 41.05 mV for $SnO_{1.92}$@Cu and 72.38 mV for Cu foil. This can be ascribed to the promoted Zn nucleation on the $SnO_{1.17}$@Cu substrate.

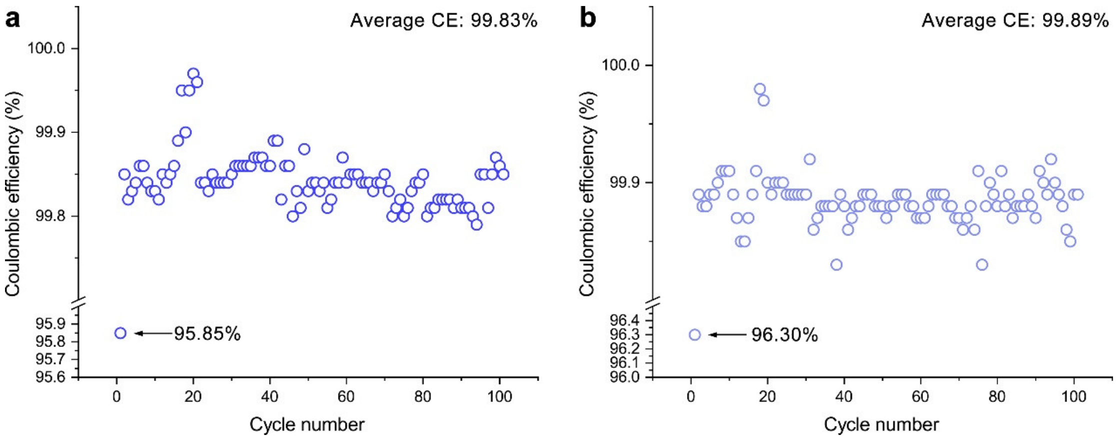

Figure S17. Coloumbic efficiency of measured by (a) the general plating/stripping method and (b) Aurbach method.

(1) The CE was measured using the most common method, where 0.1 mAh cm^{-2} of Zn metal was plated under a current density of 0.1 mA cm^{-2} onto a Cu substrate (denoted by the charge passed in the external circuit, Qp), followed by stripping the deposited Zn metal to a cut-off voltage of 0.5 V. This voltage signifies the removal of all accessible Zn, as represented by the charge Qs. The CE for each cycle was calculated using the following equation:

$$CE = \frac{Q_s}{Q_p}$$

As shown in Figure S17a, the $SnO_{1.17}$@Cu||Zn half-cell exhibited an initial CE of 95.85% and an average CE of 99.83% from the 2nd to the 100th cycles, suggesting the high reversibility of the Zn^{2+} plating/stripping process in $SnO_{1.17}$@Zn.

(2) The Aurbach method has been employed to exclude the conversion reaction between Zn and the Cu substrate surface (e.g., $Cu_2O + Zn^{2+} + 2e^- \rightarrow 2Cu^0 + ZnO$). In this method, a given amount of charge of 1 mAh cm-2 is used to deposit Zn onto the Cu substrate first as a Zn reservoir, then a smaller portion of the charge of 0.1 mAh cm-2 is used to cycle Zn between working and counter electrodes for multiple cycles under 0.1 mA cm-2. After cycling, a final exhaustive strip of the remaining Zn reservoir is performed to the cut-off voltage of 0.5 V. The results have been demonstrated in Figure S17b, where the average CE calculated by the Aurbach method is 99.89%, which is slightly higher than the 99.83% from the first method potentially due to the elimination of the reaction between the Zn and Cu electrodes. The high average CE measured by the Aurbach method further validates the highly reversible Zn^{2+} plating/stripping process of the $SnO_{1.17}$@Zn Anode.

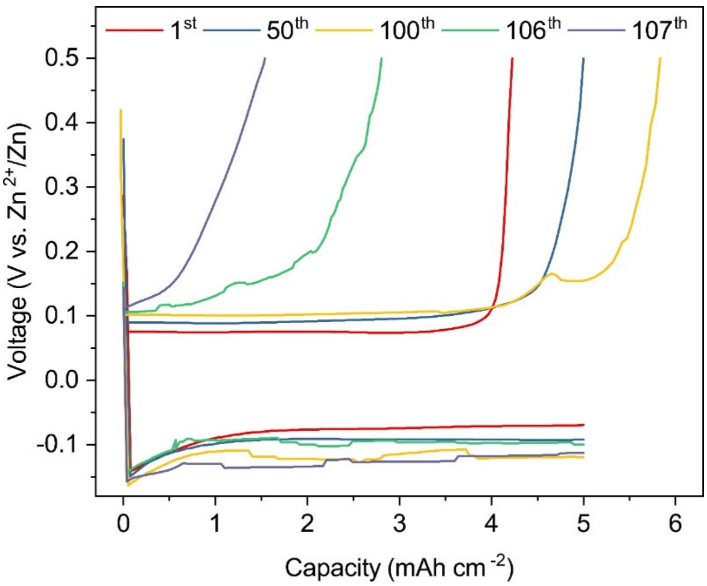

Figure S18. Selected charge-discharge profiles of the pristine Zn||Cu cell.

The cell based on pristine Zn displays fluctuating voltage profiles after only 50 cycles and a drastically degraded charge capacity at 106th and 107th, which decreases the Coulombic efficiency of the Zn||Cu cell, resulting in cell failure. The unstable cycling behavior is ascribed to the severe water erosion on the electrode.

Number	**Refs.**	**Current density ($mA\ cm^{-2}$)**	**Capacity ($mAh\ cm^{-2}$)**	**Lifespan (h)**	**Thickness of the coating layer**	**Zn utilization ratio (%)**
1	[8]	5	5	500	N/A	7.4
2	[9]	10	5	450	14 nm	8.5
3	[10]	10	5	800	10000 nm	11.5
4	[11]	5	5	300	300 nm	85.5
5	[12]	6.5	6.5	250	N/A	80.0
6	[13]	6.5	6.5	100	N/A	85.0
7	[14]	10	10	275	8000 nm	34.1
8	[15]	10	10	300	10000 nm	56.8
9	[16]	10	10	230	300 nm	58.0
10	[17]	2	11.6	420	N/A	90.0
11	[18]	8.85	13.35	300	N/A	34.1
12	[19]	40	20	210	N/A	75.0
13	[20]	15	20	200	N/A	80.0
14	[21]	10	20	120	N/A	80.0
This work		**20**	**20**	**600**	**~70 nm**	**85.7**
		1.5	**1.5**	**800**	**~70 nm**	**91.5**

Table S4. Comparison of electrochemical performances between this work and previous reports from the literature.

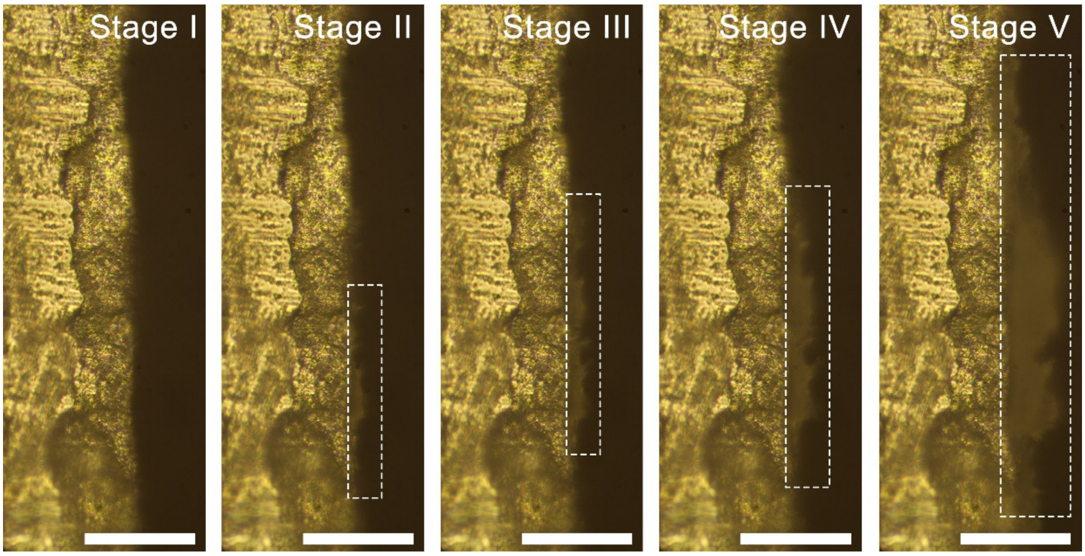

Figure S19. In-situ observation of Zn^{2+} plating at 5 mA cm^{-2} for the pristine Zn specimen via optical microscope for 1 hous (images of each stages were obtained per 15 mins). Scale bar, 100 μm.

It is observed that the plated Zn accumulates in the region marked with a white dashed box at stage II, indicating uneven Zn^{2+} plating. Subsequently, Zn^{2+} preferentially plates around the marked regions in the following stages, further promoting dendrite formation.

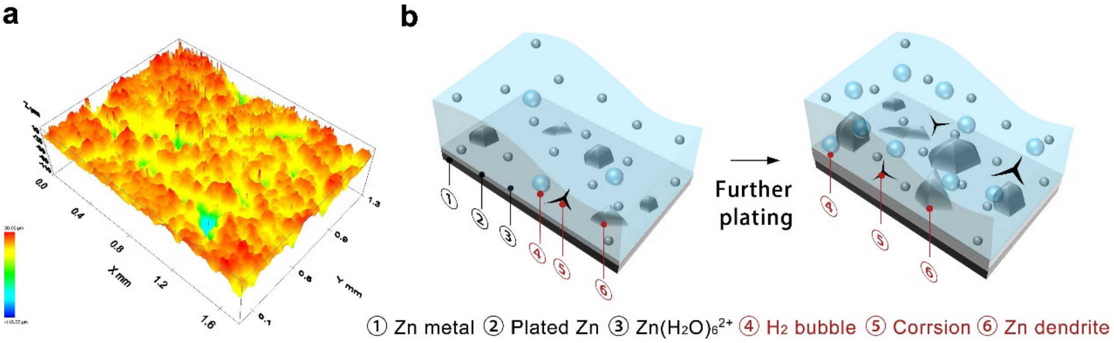

Figure S20. (a) Laser confocal microscope image of pristine Zn after Zn^{2+} plating, exhibiting a rough microstructure due to the plated Zn on top of the surface. (b) Schematic of Zn^{2+} plating on the pristine Zn.

The high surface roughness (arithmetic mean height, Sa) of 10.02 μm in pristine Zn suggests an uneven Zn^{2+} plating process, which was ascribed to the formation of Zn dendrites. The low-altitude regions (green and blue) on the Zn foil in Figure S18a may be attributed to corrosion reactions occurring on the Zn surface. As illustrated in Figure S18b, Zn dendrites were generated during stage II of Zn^{2+} plating on pristine Zn as indicated in Figure S17. The unevenness of Zn^{2+} plating and inevitable parasite reactions ultimately lead to rapid anode failure.

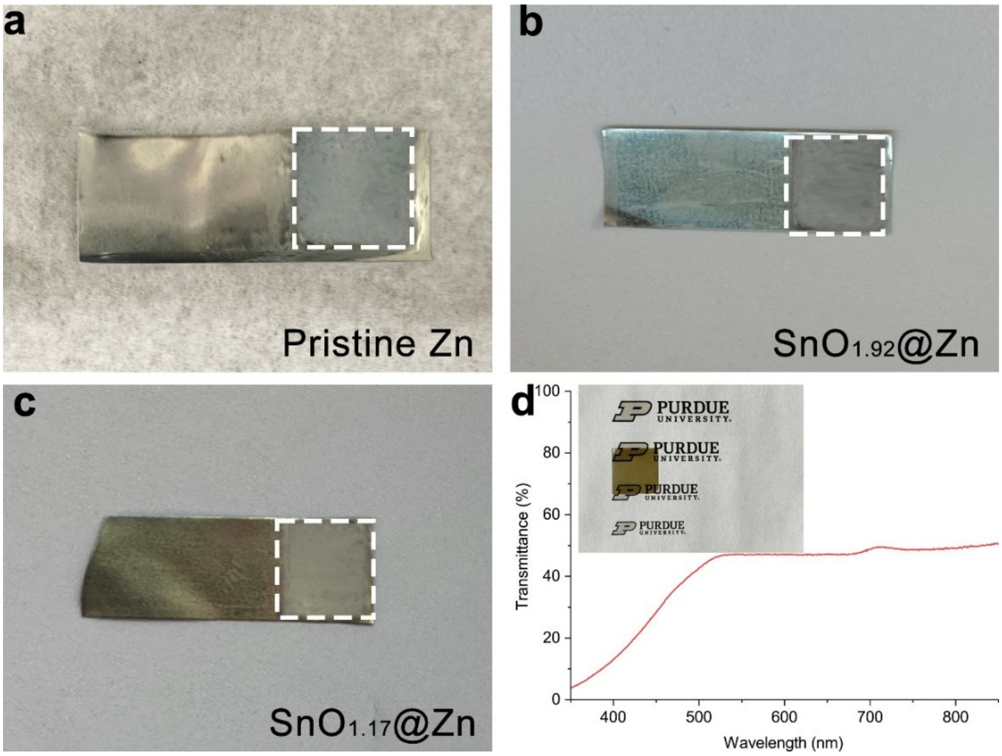

Figure S21. Optical photographs of (a) pristine Zn, (b) SnO$_{1.92}$@Zn, and (c) SnO$_{1.17}$@Zn after Zn^{2+} plating during the in-situ Zn^{2+} plating observation. (d) UV–vis optoelectronic properties of visible-regime transmittance of the SnO$_{1.17}$ interphase. Inset, the optical image of SnO$_{1.17}$-coated glass.

It can be identified that the Zn^{2+} plated region exhibited gray color (marked with the white square), which is clearly distinguished from the color of the electrode before Zn^{2+} plating. Figure S21d plots the visible-regime transparency of the SnO$_{1.17}$ films as a function of wavelengths ranging from 300 to 900 nm. The SnO$_{1.17}$ interphase exhibited transparency of approximately 50%, as demonstrated by the visibility of the "Purdue" logo and plated Zn beneath the glass coated with the SnO$_{1.17}$ interphase. This observation confirms that the SnO$_{1.17}$ interphase maintains sufficient optical transparency. This high transparency of the SnO$_{1.17}$ interphase enables the observation of a color change when Zn^{2+} plating occurs underlying the SnO$_{1.17}$ interphase. In order to further analyze the evolution of the surface composition and morphology, EDX and XRD were employed to characterize pristine Zn, SnO$_{1.92}$@Zn, and SnO$_{1.17}$@Zn anodes.

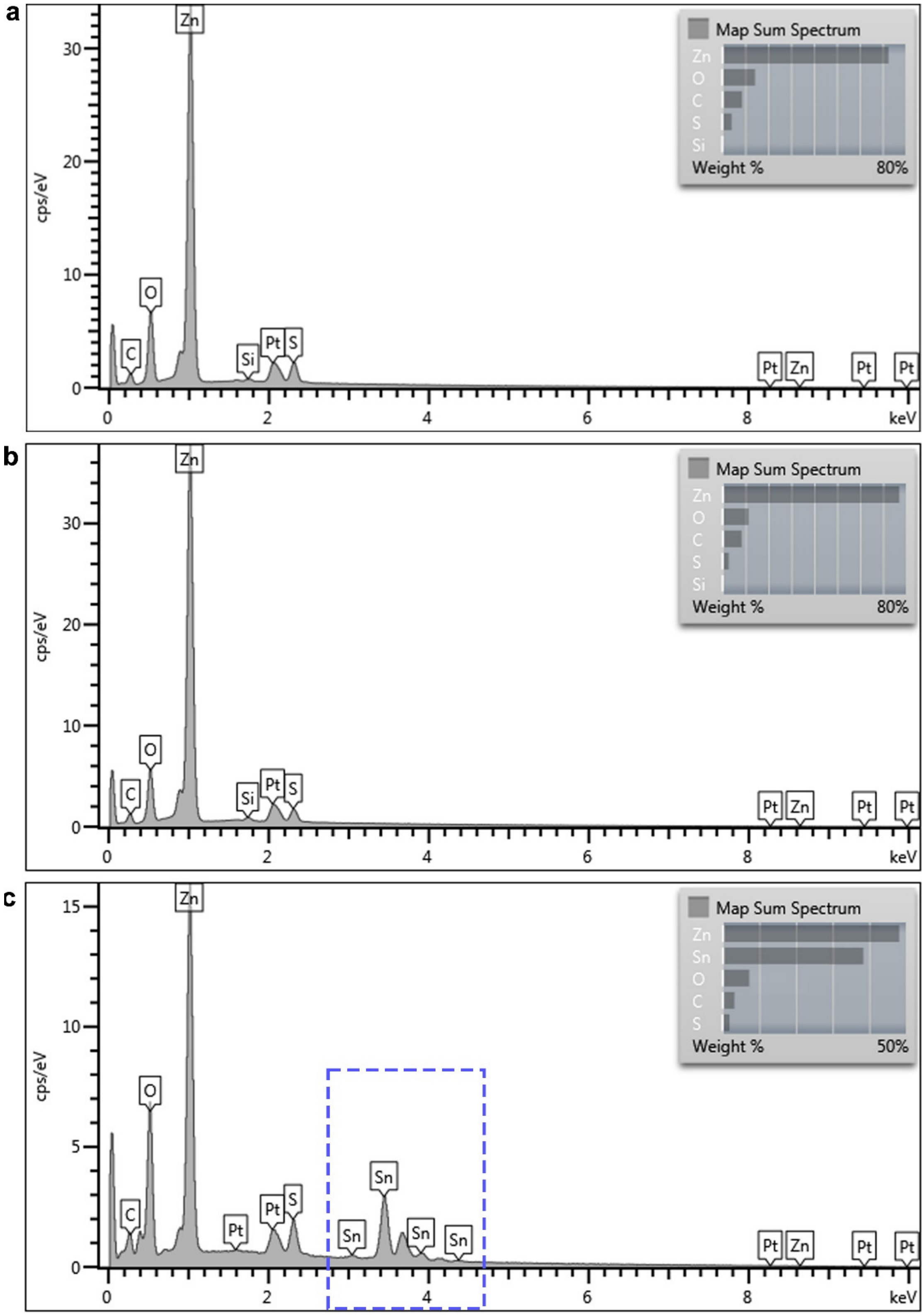

Figure S22. EDX analysis spectrum of (a) pristine Zn, (b) SnO$_{1.92}$@Zn, and (c) SnO$_{1.17}$@Zn after Zn^{2+} plating during in-situ observation

As shown in Figure S20a, peaks of Zn, O, and S are observed in pristine Zn, where the O and S may be attributed to the residual ZnSO$_4$ from the electrolyte. Peaks of Zn, O, and S also appear in SnO$_{1.92}$@Zn while the peaks related to Sn are absent in the detection depth range of EDS (~5 μm), which indicates a

Zn-plated layer of at least 5 μm covering the $SnO_{1.92}$, corroborating the on-plane Zn^{2+} plating behavior (i.e., overlying the $SnO_{1.92}$ interphase). In contrast, peaks ranging from 3 keV to 4.5 keV, which was assigned to Sn, are detected in $SnO_{1.17}$@Zn. The detection of Sn from the $SnO_{1.17}$@Zn specimen supports the underlying plating of Zn, relative to the $SnO_{1.17}$ interphase. The weight ratio of 38.6% Sn and 6.4% O corresponds to the atomic ratio of 1:1.22 of Sn:O, which is close to the atomic ratio of $SnO_{1.17}$.

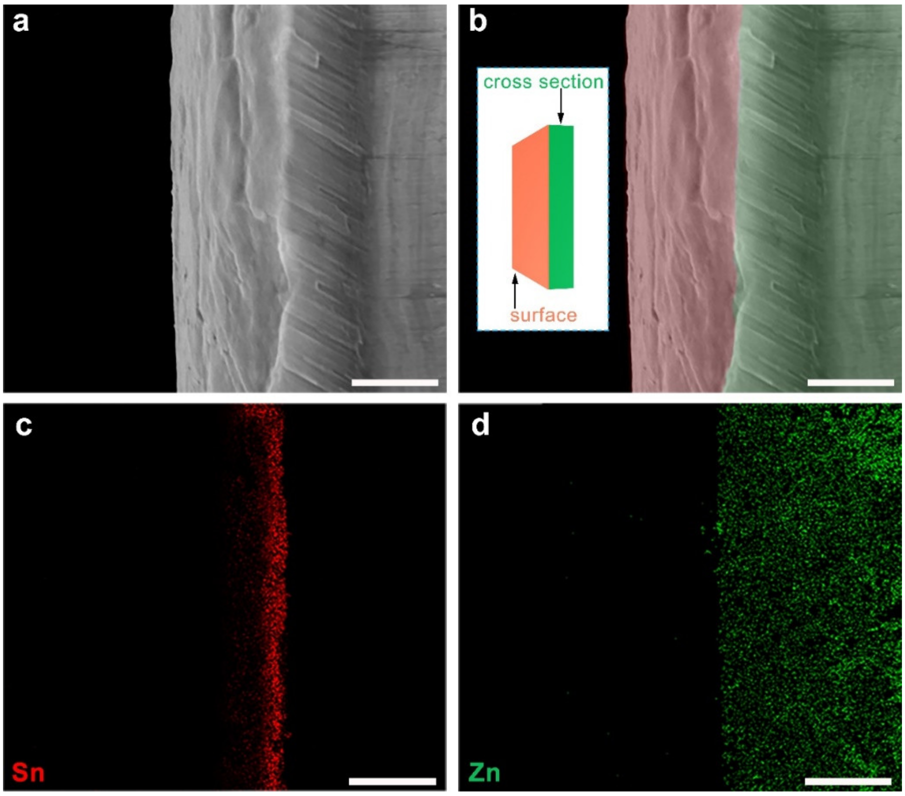

Figure S23. (a) SEM images and (b) false color images of SnO1.17@Zn anode after Zn plating. Inset, the schematic of tilted view of the SEM image. EDX mapping analysis of element Sn (c) and element Zn (d). Scale bar: 5 μm

To further confirm that the Zn^{2+} plating position lies beneath the $SnO_{1.17}$ interphase, scanning electron microscopy (SEM) and EDX mapping analyses were conducted on the $SnO_{1.17}$@Zn with plated Zn (~ 2 mAh cm^{-2}). The cross-sectional view in the SEM images was slightly tilted to show the morphology of the top surface. Figure S23a shows the cross-sectional image of the $SnO_{1.17}$@Zn anode after Zn^{2+} plating. The surface region (red) and the cross-section region (green) have been distinguished by the false color image as shown in Figure S23b. EDX analysis Figure S23c and 23d indicated that the Sn element is distributed exclusively in the surface region, while Zn is primarily distributed beneath the Sn-rich surface (i.e., $SnO_{1.17}$). These findings directly confirm that Zn^{2+} plating occurs beneath the $SnO_{1.17}$ interphase.

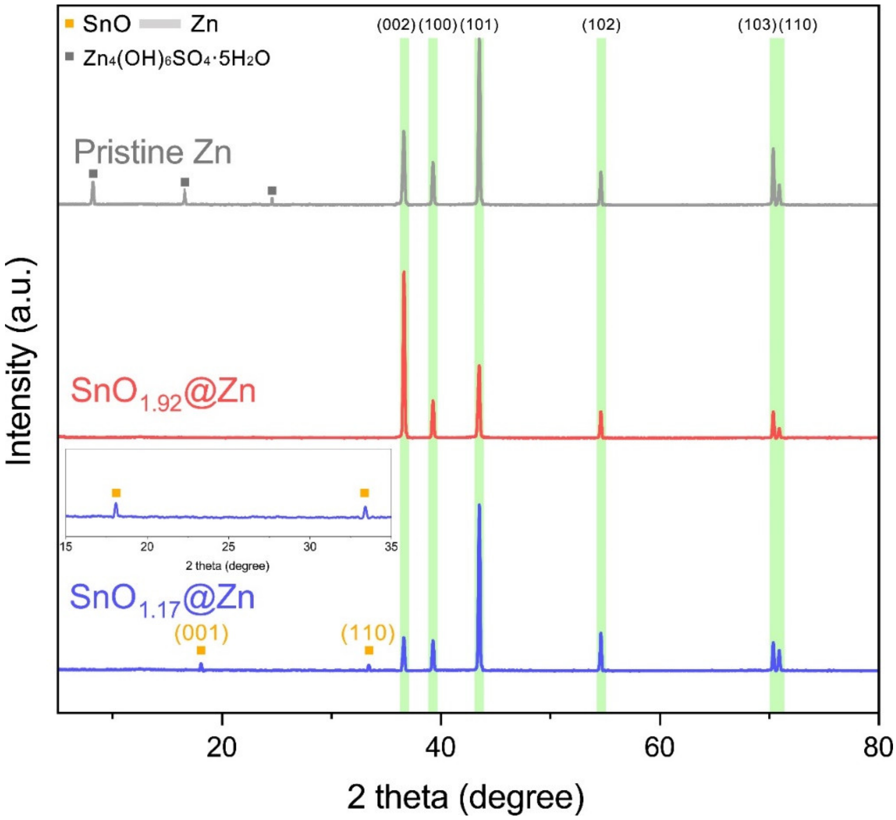

Figure S24 XRD patterns of pristine Zn, $SnO_{1.92}$@Zn, and $SnO_{1.17}$@Zn after in-situ optical observation.

It is noted that the XRD peaks located at 8.3°, 16.4°, and 24.2° are observed in pristine Zn are attributed to the by-product, $Zn_4SO_4(OH)_6$ •$5H_2O$. In contrast, the $Zn_4SO_4(OH)_6$ •$5H_2O$ was not detected in $SnO_{1.17}$@Zn and $SnO_{1.92}$@Zn. XRD patterns of $SnO_{1.17}$@Zn show two peaks located at 2 theta diffraction angles of 18.1 and 33.4°, which are ascribed to the (001) and (110) facets of SnO, as discussed in Figure 1c, further validating Zn^{2+} plating underlying the $SnO_{1.17}$ interphase. It should be noted that the dominant Zn peak in $SnO_{1.92}$@Zn and $SnO_{1.17}$@Zn is different: Zn (002) for $SnO_{1.92}$@Zn and Zn (101) for $SnO_{1.17}$@Zn, which indicates different preferential growth depending on the Sn-O phase, which aligns with the results shown in Figure 5f and 5g.

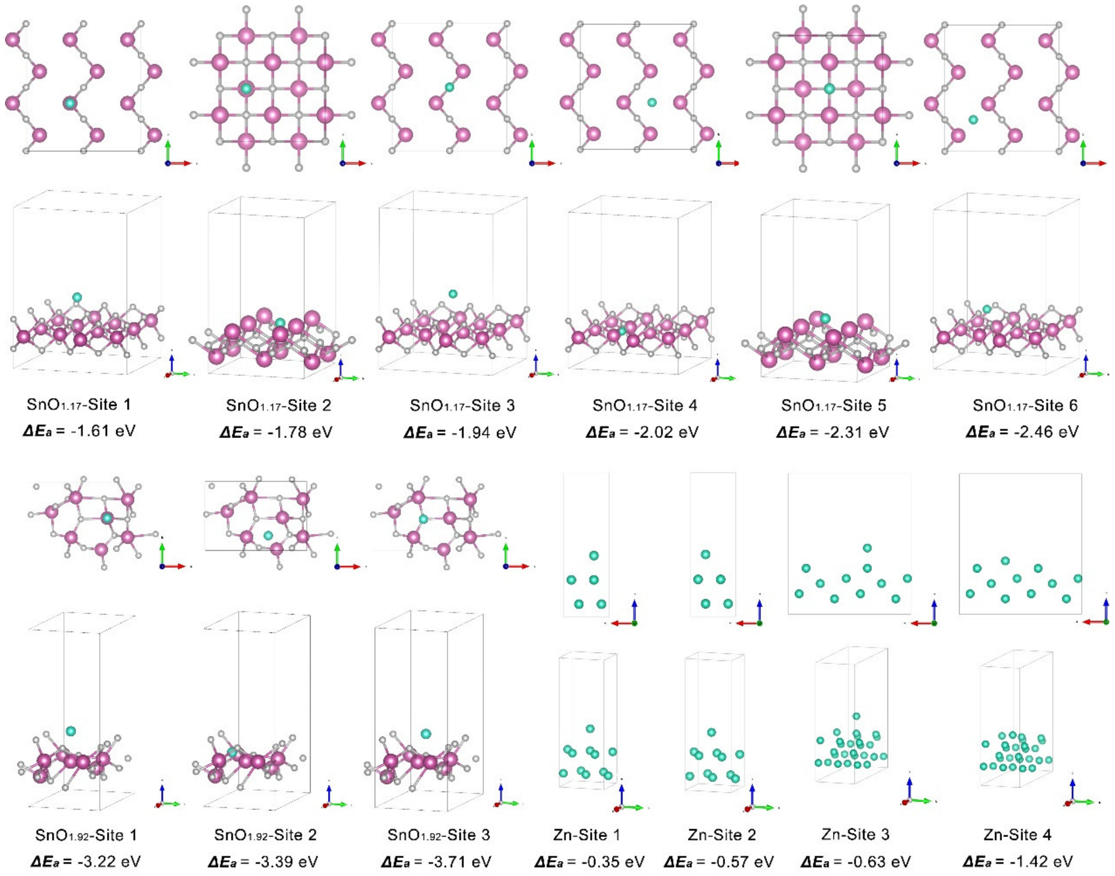

SnO$_{1.17}$-Site 1 ΔE_a = -1.61 eV

SnO$_{1.17}$-Site 2 ΔE_a = -1.78 eV

SnO$_{1.17}$-Site 3 ΔE_a = -1.94 eV

SnO$_{1.17}$-Site 4 ΔE_a = -2.02 eV

SnO$_{1.17}$-Site 5 ΔE_a = -2.31 eV

SnO$_{1.17}$-Site 6 ΔE_a = -2.46 eV

SnO$_{1.92}$-Site 1 ΔE_a = -3.22 eV

SnO$_{1.92}$-Site 2 ΔE_a = -3.39 eV

SnO$_{1.92}$-Site 3 ΔE_a = -3.71 eV

Zn-Site 1 ΔE_a = -0.35 eV

Zn-Site 2 ΔE_a = -0.57 eV

Zn-Site 3 ΔE_a = -0.63 eV

Zn-Site 4 ΔE_a = -1.42 eV

Figure S25. Models used for calculating the adsorption energy of one Zn adsorption at different conditions.

SnO$_{1.17}$	site 1	(001) facet, on top of the Sn atom
	site 2	(101) facet, on top of the Sn atom
	site 3	(101) facet, on top of the O atom
	site 4	(101) facet, hollow site between two Sn atoms
	site 5	(001) facet, on top of the O atom
	site 6	(101) facet, hollow site between two O atoms
SnO$_{1.92}$	site 1	on top of the Sn atom
	site 2	hollow site among three O atoms
	site 3	on top of the O atom
Zn	site 1	(002) facet, on top of the Zn atom
	site 2	(002) facet, hollow site between two Zn atoms
	site 3	(101) facet, on top of the Zn atom
	site 4	(101) facet, hollow site between two Zn atoms

Table S5. Detailed information on selected sites for DFT adsorption energy calculations.

To systematically evaluate the adsorption behavior of the Zn atom on SnO$_{1.17}$, SnO$_{1.92}$, and Zn metal, top and hollow adsorption models were considered for DFT calculations. A detailed description of each selected site has been provided in Table S3. For the case of Zn metal, the Zn atom likely adsorbs on site 4 of (101) facet in Zn metal due to the lowest adsorption energy (-1.42 eV). For SnO$_{1.17}$, the Zn atom tends to preferentially adsorb on site 4 of the (101) facet of $SnO_{1.17}$ due to the lowest adsorption energy of -2.46 eV as indicated in Figure S22. For the $SnO_{1.92}$, the Zn atom prefers to adsorb on site 3 (on the top of the O atom) with a lower adsorption energy of -3.71 eV compared to the -3.22 eV of site 1 and -3.39 eV of site 2.

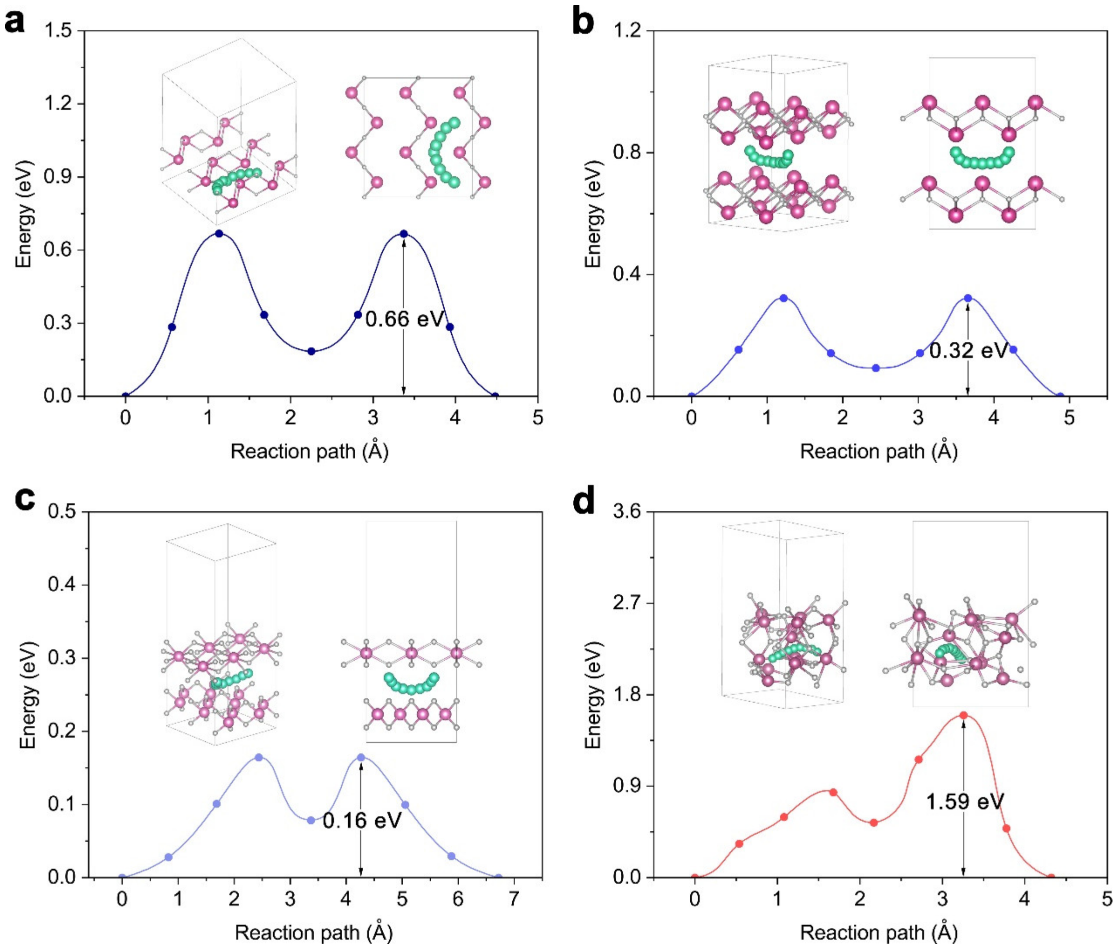

Figure S26. NEB calculation of the diffusion barrier of a Zn atom (green symbols) as a function of structure and orientation of tin oxides. The Zn atom diffusion barrier in (a) the (101) facet of SnO, (b) the (001) facet of SnO, (c) the grain boundary between (101) and (001) facet of SnO, and (d) the amorphous SnO_2. The inserts show the diffusion pathways.

The climbing image nudged elastic band (CI-NEB) method was used to quantify the energy barrier that a Zn atom is required to migrate in the considered material system of tin oxides as a function of structure and orientation. The migration barriers for a Zn atom diffusion along the (101) facet, the (001) facet, and the grain boundary of SnO are only 0.66 eV, 0.32 eV, and 0.16 eV as indicated in Figure S23a, S23b, and S23c. In contrast, the preferred migration energy barrier calculated is 1.59 eV for a Zn atom diffusion along the amorphous SnO_2 across multiple Zn sites shown in Figure S23d (green sphere). The average distance between the Zn atom and the O atoms of minimum energy path (MEP) in amorphous SnO_2 is 1.62 Å, which is smaller than the 1.89 Å of SnO (101), 2.06 Å of SnO (001), and 2.43 Å of the grain boundary of SnO, resulting in a stronger interaction between the Zn atom and O atoms during the migration within the amorphous SnO_2, which limits the overall migration process, compared to that of SnO. Moreover, there are seven O atoms involved in the MEP in SnO_2 to interact with the Zn^{2+}, which is higher than the four O atoms of the SnO (101) facet, six O atoms of SnO (001) facet, and five O atoms of the grain boundary of SnO, forming more Zn-O interactions. Overall, more and stronger Zn-O interactions in amorphous SnO_2 require much higher migration energy of Zn^{2+} than that of SnO and limit the diffusion of Zn^{2+} through the SnO_2. Therefore, Zn is more likely plated on top of the surface of $SnO_{1.92}$@Zn. In contrast, the significantly lower migration energy required for Zn^{2+} diffusion in SnO enables the Zn^{2+} plating underneath the $SnO_{1.17}$ used in this study. According to the DFT calculations considering various sites in SnO, the preferrable diffusion path of Zn^{2+} in SnO (i.e., $SnO_{1.17}$ in our study) is most likely the grain boundaries between the SnO (101) and (001) orientations with the lowest barrier energy of 0.16 eV.

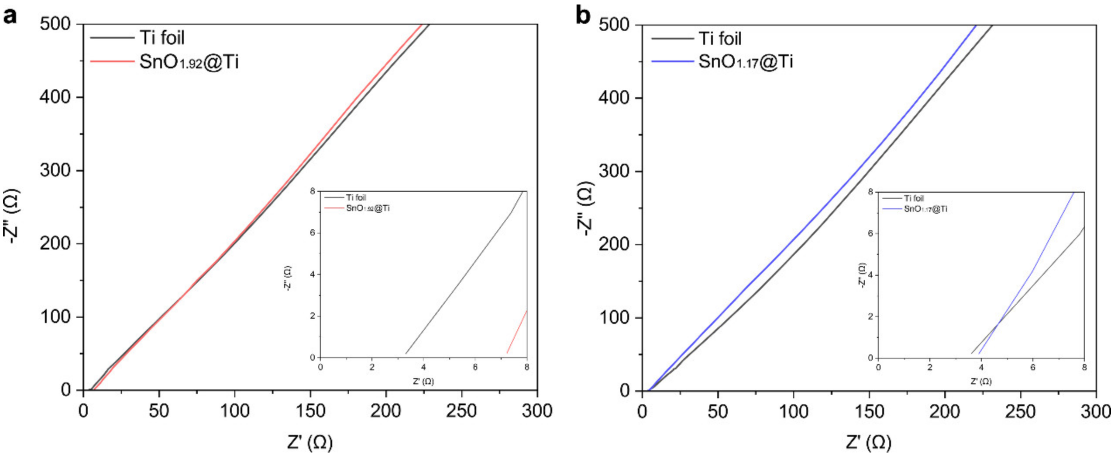

Figure S27. Nyquist plots of (a) $SnO_{1.92}$@Ti||glass fiber||Ti and (b) $SnO_{1.17}$@Ti||glass fiber||Ti configuration over the frequency range of 100 kHz to 0.1 Hz. Insets show enlarged profiles.

The ionic conductivity (σ) can be evaluated according to the following equation:

$$\sigma = \frac{L}{R_b S}$$

where R_b represents the resistance based on the EIS measurement, L represents the thickness of the $SnO_{1.92}$ and $SnO_{1.17}$ coating layers, and S is the contact area between the electrode and electrolyte (1.13 cm^{-2}). For the $SnO_{1.92}$@Ti//glass fiber//Ti cell, the $R_{b(SnO1.92)} = R_b - R_{b(glass\ fiber)} = 3.86\ \Omega$ at room temperature. For the $SnO_{1.17}$@Ti//glass fiber//Ti cell, the $R_{b(SnO1.17)} = R_b - R_{b(glass\ fiber)} = 0.31\ \Omega$ at room temperature. Therefore, the ionic conductivity of $SnO_{1.92}$ and $SnO_{1.17}$ layers are estimated to be 8.72×10^{-7} mS cm^{-1} and 1.36×10^{-4} mS cm^{-1}, respectively. The ionic conductivity of the $SnO_{1.17}$ coating layer is about 156 times higher than the $SnO_{1.92}$ coating layer.

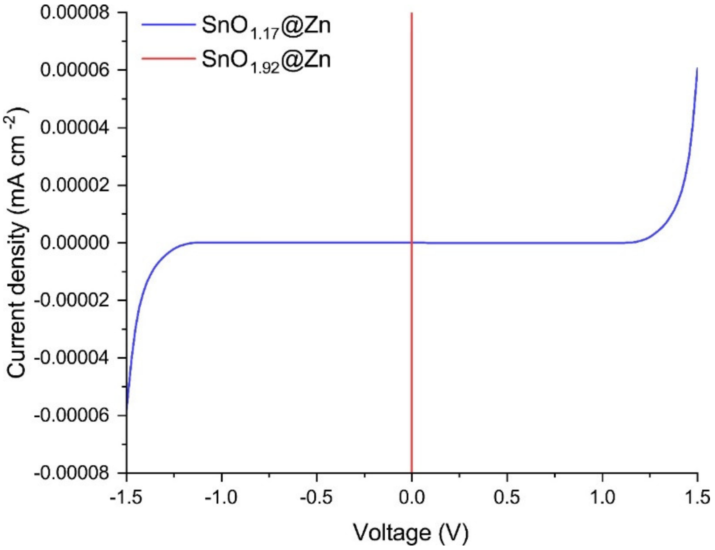

Figure S28. Extended I-V curve of Figure 5c

The enlarged I-V curve exhibits the characteristics of a Schottky contact (non-linear I–V curve) at the $SnO_{1.17}$/Zn interface, attributed to the contact behavior Zn (Φ=4.3 eV) and p-type $SnO_{1.17}$ (Φ=5.42 eV) and the resulting Schottky barrier height of 1.1 eV. However, Ohmic characteristics (i.e., linear I–V curves) are observed at the $SnO_{1.92}$/Zn interface.

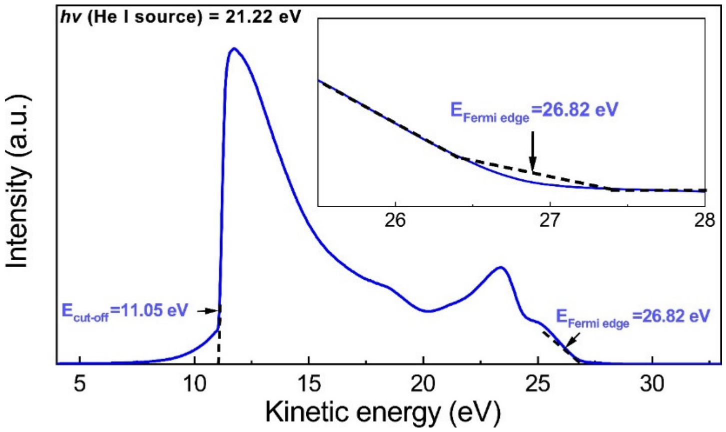

Figure S29. UPS spectra measured from the $SnO_{1.17}$ interphase.

The work function (Φ) is determined using ultraviolet photoelectron spectroscopy (UPS) with a photon energy of 21.22 eV (from He I source). It is calculated using the cutoff kinetic energy ($E_{cut-off}$), which corresponds to the energy of free electrons generated by the photoelectric effect, and the Fermi edge position ($E_{Fermi-edge}$) via the equation

$$\Phi = h\nu + E_{cut-off} - E_{Fermi-edge}$$

The UPS results for $SnO_{1.17}$ are presented in Figure S25, showing a cutoff kinetic energy of approximately 11.05 eV. An enlarged spectrum (with kinetic energy ranging from 25 to 28 eV) is included as an inset in Figure S26, where the Fermi edge location of $SnO_{1.17}$ is estimated to be around 26.82 eV. Based on the determined $E_{cut-off}$ and $E_{Fermi-edge}$ positions, the Φ of the $SnO_{1.17}$ interphase in this study is calculated to be 5.45 eV. The work functions of $SnO_{1.92}$ and Zn, which are well-established materials, compared to SnO, are taken to be 4.53 eV and 4.3 eV, respectively, from previous reports.[22]

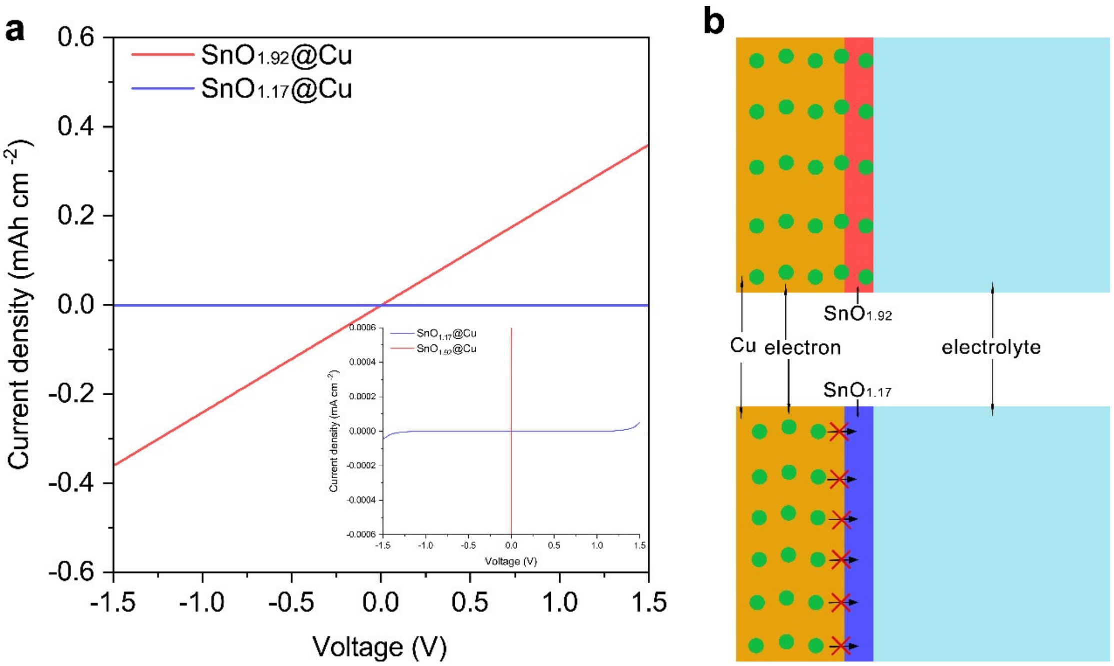

Figure S30. (a) I-V curves of $SnO_{1.92}$ and $SnO_{1.17}$ interphases with Cu foil. Inset, enlarged I-V curve. (b) Schematic of electron transmission in $SnO_{1.92}$@Cu and electron isolation in $SnO_{1.17}$@Cu.

Current-voltage (I–V) characteristics were measured to determine the type of contact formed at the $SnO_{1.17}$/Cu and $SnO_{1.92}$/Cu interfaces. The I–V curve in Figure S27a demonstrates the characteristics of a Schottky contact (non-linear I–V curve) at the $SnO_{1.17}$/Cu interface, attributed to the contact behavior Cu (Φ=4.6 eV) and p-type $SnO_{1.17}$ ($\Phi = 5.45$ eV) with a Schottky barrier height of 0.85 eV. In contrast, the $SnO_{1.92}$/Cu interface shows non-rectifying ohmic characteristics (i.e., linear I–V curves). During the Zn^{2+} plating process, the electron will pass through and reach the surface of the $SnO_{1.92}$ layer as visualized in Figure S27 (upper). However, the electrons were unable to be transferred through the $SnO_{1.17}$ and were limited in the Cu during the Zn^{2+} plating process as illustrated in Figure S26b (lower).

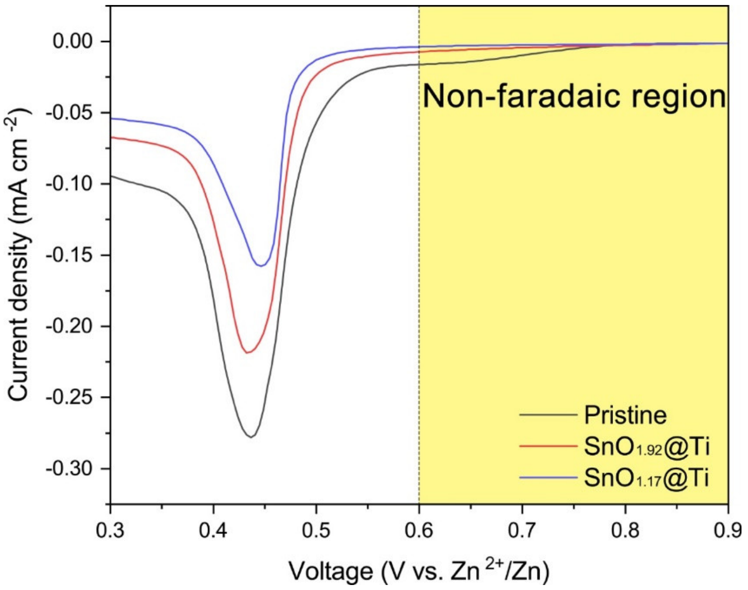

Figure S31. Extended plots in Figure 3b at lower voltage regime.

There are no distinct redox peaks that are observed in the range from 0.6-0.9 V (vs. Zn^{2+}/Zn) in CV measurements for all three samples. The dominating electrochemical process within this voltage range (marked in yellow) is considered a non-faradaic process, which is mainly contributed by the electric double layer (EDL) capacitance adsorption of the charge carrier.[23]

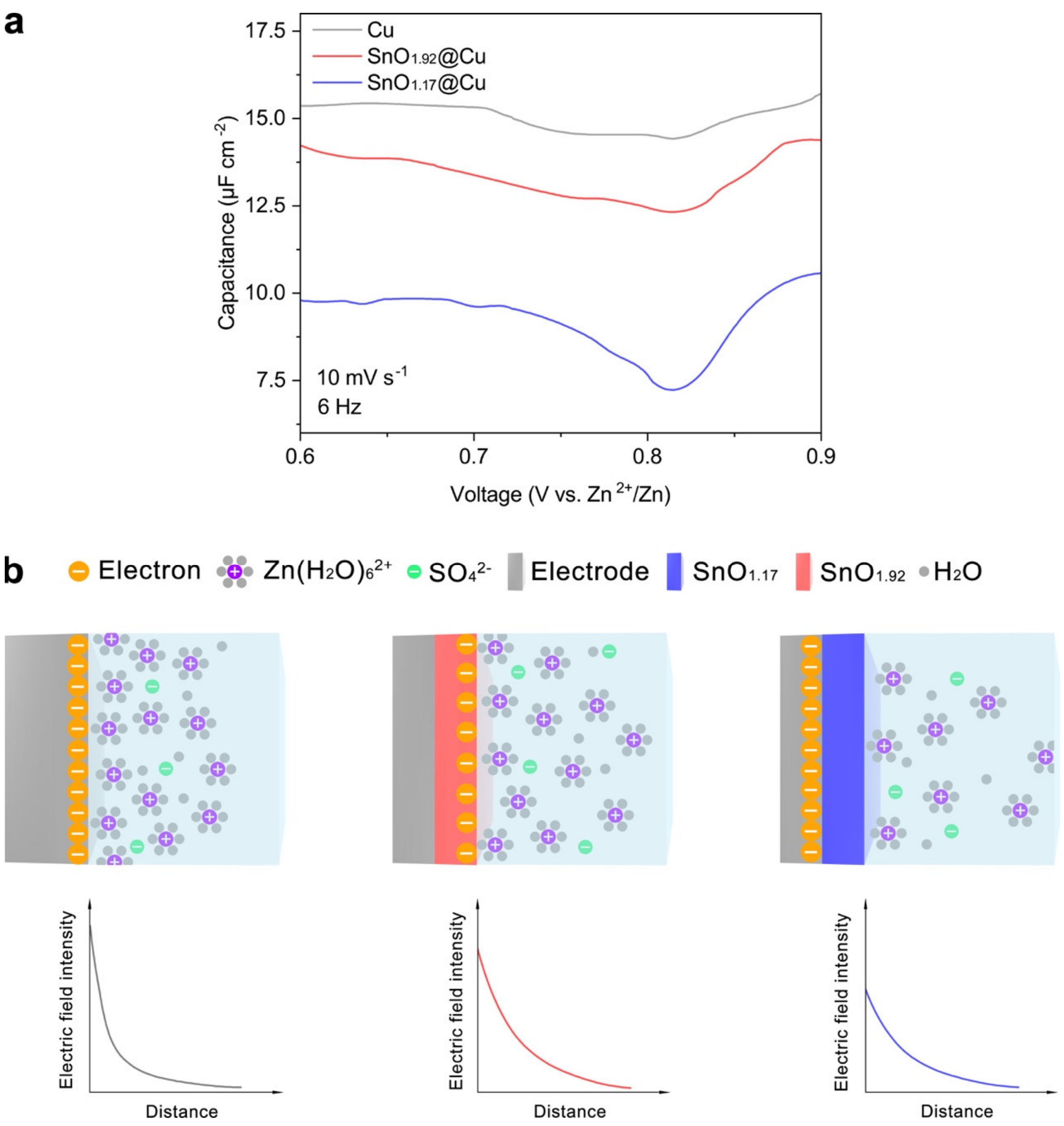

Figure S32. Non-Faradaic capacitance-potential curves for the pristine Cu, $SnO_{1.92}$@Cu, and $SnO_{1.17}$@Cu anodes.

The non-Faradaic EDL capacitance adsorption of pristine Cu, $SnO_{1.92}$@Cu, and $SnO_{1.17}$@Cu anodes were quantified through the AC voltammetry as indicated in Figure S29a. The capacitance of pristine Cu is higher than that in cells with $SnO_{1.92}$@Cu, and $SnO_{1.17}$@Cu anodes, which is attributed to the direct contact between the metal anode and the aqueous electrolyte. The $SnO_{1.92}$ interphase exhibited a lower capacitance value compared with pristine Cu, indicating the less accumulated electron at the surface of $SnO_{1.92}$@Cu compared to pristine Cu (Figure S29b). For $SnO_{1.17}$@Cu, the electron transfer was inhibited in the Cu as indicated in Figure S29c, attributed to the p-type behavior of $SnO_{1.17}$ and the non-ohmic contact nature at the $SnO_{1.17}$/Cu interface. Consequently, the $SnO_{1.17}$@Cu delivered the lowest capacitance at the non-faradaic region, contributing to the lower Zn^{2+} migration barrier at the inner Helmholtz plane.

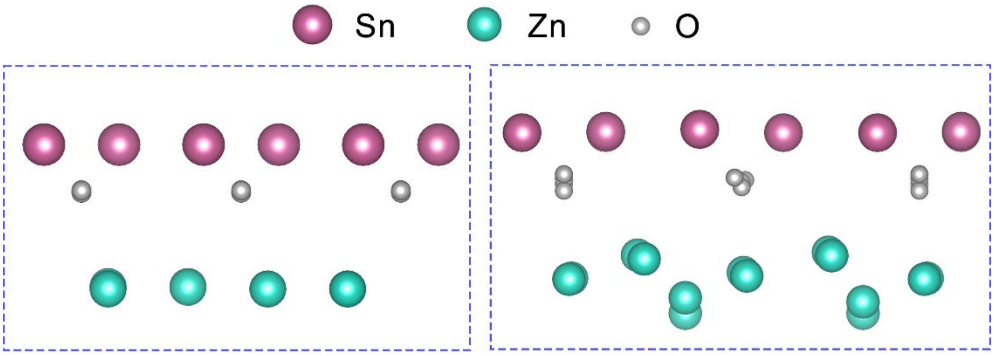

SnO$_{1.17}$ (110)@Zn (002)
Surface energy of Zn (002): 0.84 eV

SnO$_{1.17}$ (110)@Zn (101)
Surface energy of Zn (101): 0.74 eV

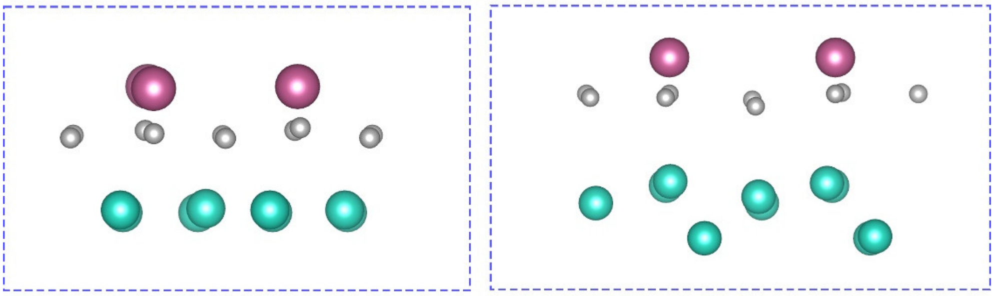

SnO$_{1.17}$ (001)@Zn (002)
Surface energy of Zn (002): 0.71 eV

SnO$_{1.17}$ (001)@Zn (101)
Surface energy of Zn (101): 0.76 eV

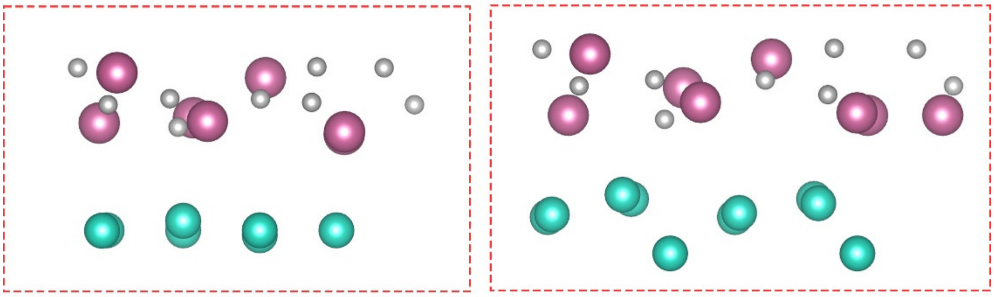

SnO$_{1.92}$ @Zn (002)
Surface energy of Zn (002): 0.30 eV

SnO$_{1.92}$ @Zn (101)
Surface energy of Zn (101): 1.12 eV

Figure S33. Calculations models for surface energy of Zn (002) and Zn (110) with polycrystalline SnO$_{1.17}$ and amorphous SnO$_{1.92}$

The surface energy of Zn (002) and Zn (101) with SnO$_{1.17}$ and SnO$_{1.92}$ interphases was calculated based on the models above. SnO1.17 (110) could effectively lower the surface energy of Zn (101) compared to SnO$_{1.17}$ (001) and amorphous SnO$_{1.92}$, implying the potential of facilitating the preferential growth of Zn (101). In contrast, SnO$_{1.92}$ successfully reduces the surface energy of Zn (002), promoting the oriented-(002) Zn^{2+} plating.

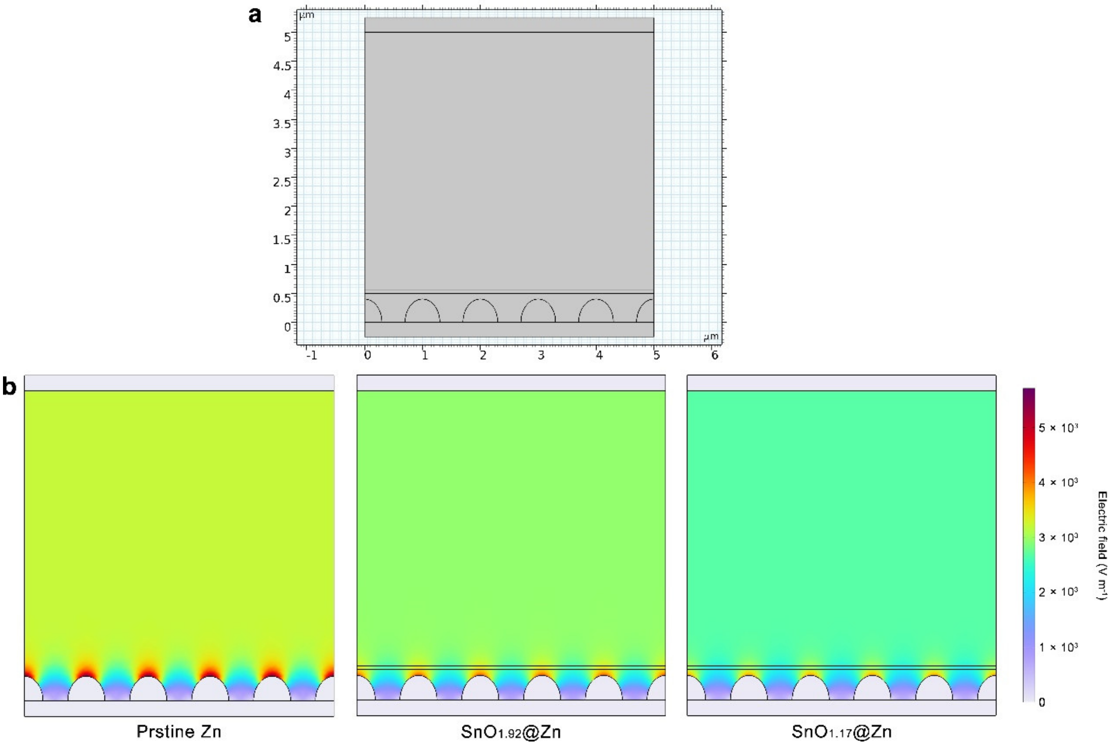

Prstine Zn

$SnO_{1.92}$@Zn

$SnO_{1.17}$@Zn

Figure S34. (a) The model cell used for finite element analysis. (b) Electric field distribution of pristine Zn electrode, $SnO_{1.92}$@Zn electrode, and $SnO_{1.17}$@Zn electrode.

The electric field distribution and Zn^{2+} concentration on pristine Zn electrode, $SnO_{1.92}$@Zn electrode, and $SnO_{1.17}$@Zn electrode are investigated by finite element analysis. In the model cell, the length and width are set to 5 and 5 μm, respectively, and the humps with a height of 0.4 μm represent the initial Zn grains as indicated in Figure S31a. The electric field tends to accumulate on the tip of these humps, which brings a high risk of dendrite growth. The presence of the $SnO_{1.17}$ interphase can equalize the electric field distribution on Zn compared to the $SnO_{1.92}$@Zn and pristine Zn due to the higher ionic conductivity and restricted electron transfer in the $SnO_{1.17}$ interphase, which decreased the trending of Zn^{2+} concentrated on the humps of the Zn anode, leading to a more uniform Zn^{2+} plating.

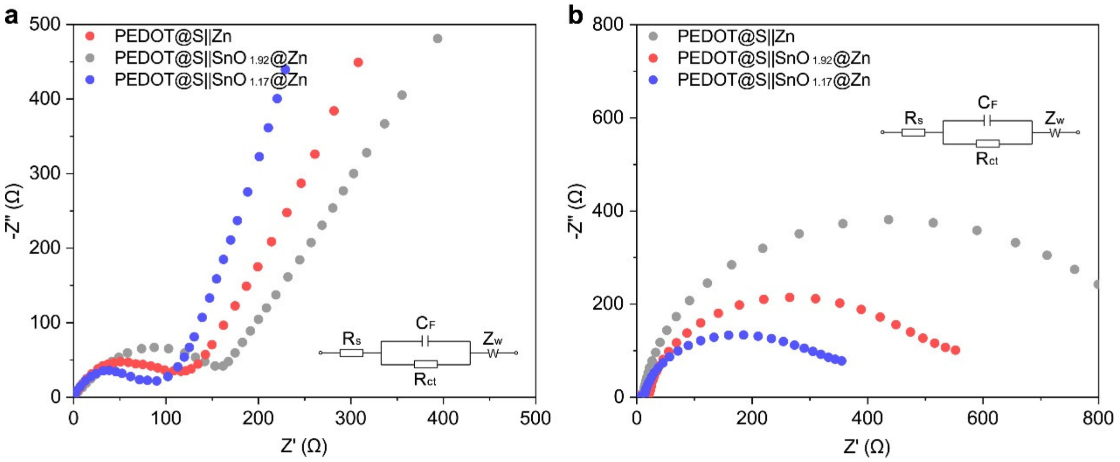

Figure S35. EIS spectra of the PEDOT@S||Zn, PEDOT@S||$SnO_{1.92}$@Zn, and PEDOT@S||$SnO_{1.17}$@Zn cells (coin-type) (a) before and (b) after cycling 600 times under 0.5 A g^{-1}. The insets are equivalent circuits used in the fitting process.

An equivalent circuit is used to simulate the resistances of three full cells with pristine Zn anode, $SnO_{1.92}$@Zn anode, and $SnO_{1.17}$@Zn anode, where Rs is the ohmic resistance of solution and electrodes, Rct is the charge transfer resistance, C_F is the double-layer capacitance, and Z_W is the Warburg impedance. Three cells exhibited close resistance before circulation while the resistance of the PEDOT@S||$SnO_{1.17}$@Zn cell is relatively lower compared to the other two counterparts. However, huge differences in the resistance of the three cells measured after circulation can be observed. The Rct of the PEDOT@S||$SnO_{1.17}$@Zn cell is 317 Ω after circulation, which is much lower than the 487 Ω measured from the PEDOT@S||$SnO_{1.92}$@Zn cell and less than half of the 834 Ω in the PEDOT@S||Zn cell.

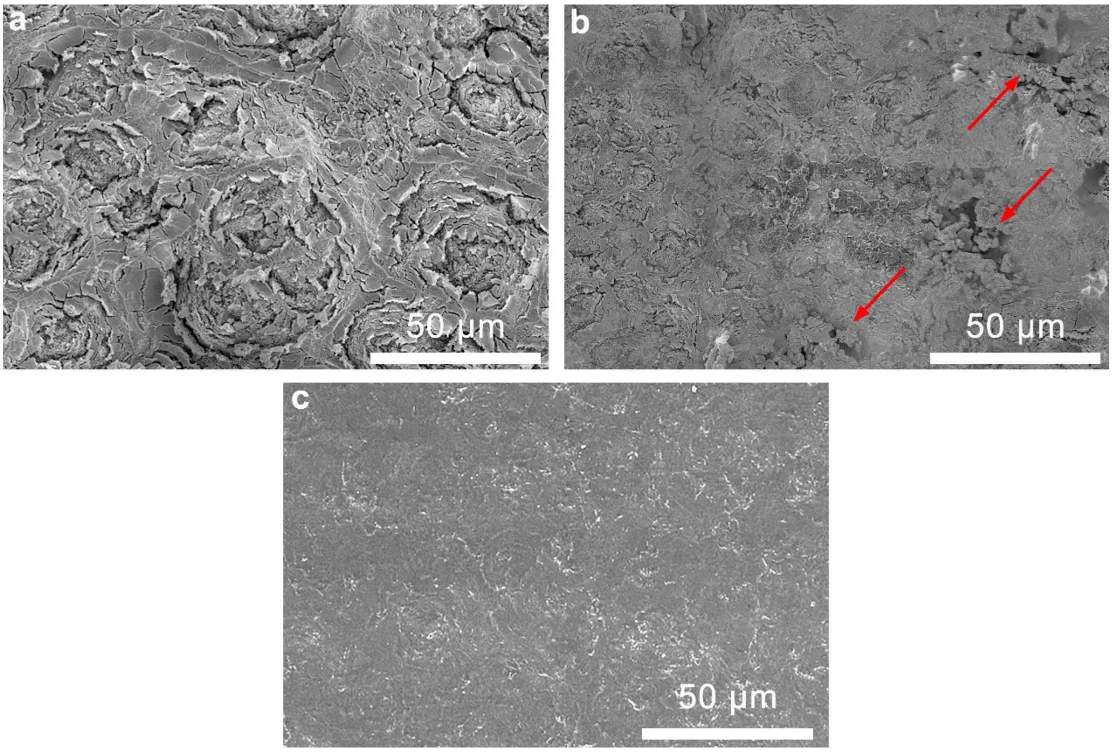

Figure S36. SEM images of pristine Zn anode, $SnO_{1.92}$@Zn anode, and $SnO_{1.17}$@Zn anode in Zn||S cells after circulation. (a) Pristine Zn anode after 357 cycles. (b) $SnO_{1.92}$@Zn anode and (c) $SnO_{1.17}$@Zn anode after 600 cycles.

The pristine Zn anode exhibited a highly rough surface with distinct protrusions and cracks as depicted in Figure S33a, which was attributed to the uneven Zn plating as well as the corrosion process. $SnO_{1.92}$@Zn anode showed a relatively smooth surface morphology compared to the pristine Zn anode (Figure S33b). However, cavities (marked with red arrows) and accumulated non-uniform products can be observed after 600 times circulation, which was associated with the inevitable corrosion of the Zn anode due to the exposure of plated Zn. In contrast, a uniform and dense surface can be observed in Figure S33c, which indicates the effectiveness of the $SnO_{1.17}$ coating layer in regulating the Zn plating process during the entire cycling test.

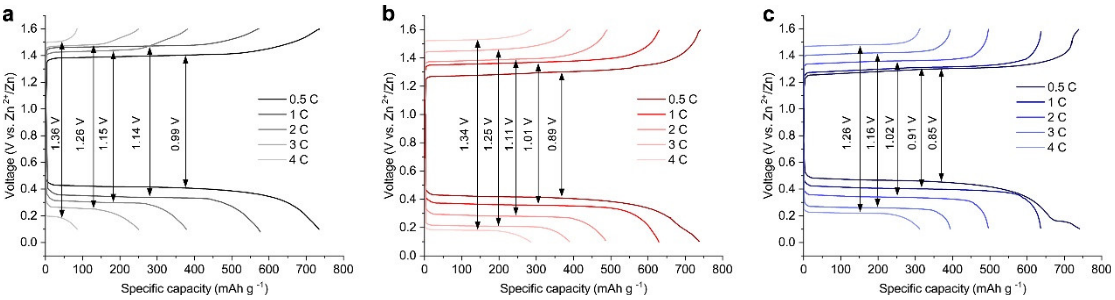

Figure S37. Charge-discharge profiles of (a) PEDOT@S||Zn, (b) PEDOT@S||$SnO_{1.92}$@Zn, and (c) PEDOT@S||$SnO_{1.17}$@Zn cells at different rates.

Figure S34 compares the charge-discharge curves of PEDOT@S||Zn, PEDOT@S||$SnO_{1.92}$@Zn, and PEDOT@S||$SnO_{1.17}$@Zn cells at a current density of 0.5 A g^{-1}, 1 A g^{-1}, 2 A g^{-1}, 3 A g^{-1}, and 4 A g^{-1}. The PEDOT@S||$SnO_{1.17}$@Zn cell delivered higher specific capacity and a smaller voltage hysteresis under various current densities compared to that in PEDOT@S||Zn cell and PEDOT@S||$SnO_{1.92}$@Zn cell, showing the improvement in the kinetics of the cell when $SnO_{1.17}$ coating layer is applied.

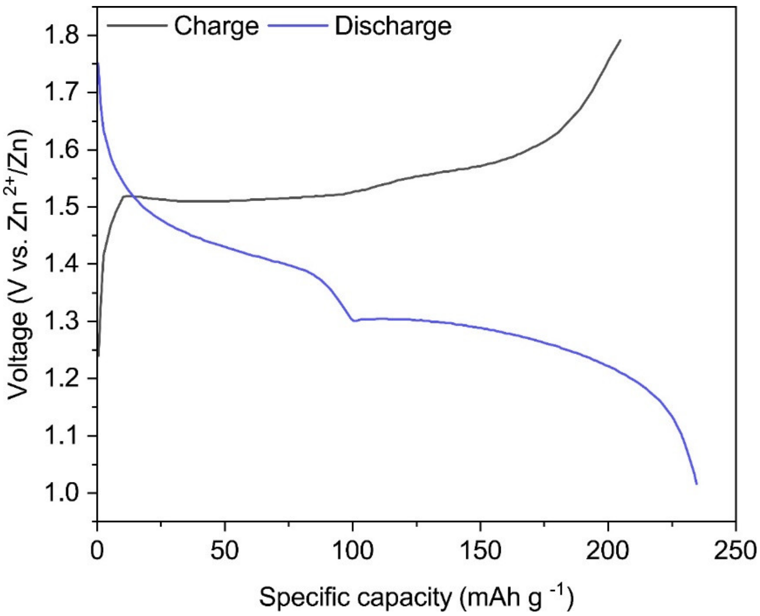

Figure S38. The charge-discharge profile of as-synthesized MnO_2 cathode materials paired with pristine Zn metal anode under 0.1 A g^{-1}.

The MnO_2 cathode materials delivered a specific capacity of more than 225 mAh g^{-1} under a current density of 0.1 A g^{-1}, which is well aligned with the previously reported specific capacity of β-MnO_2.[24] The discharge profile shows a slopping plateau at ~1.25 V, which corresponds to the Zn intercalation in the layered Zn-buserite phase.[24] The reversible Zn insertion/extraction process accounts for the electrochemical Zn storage in the cell cycling performance.

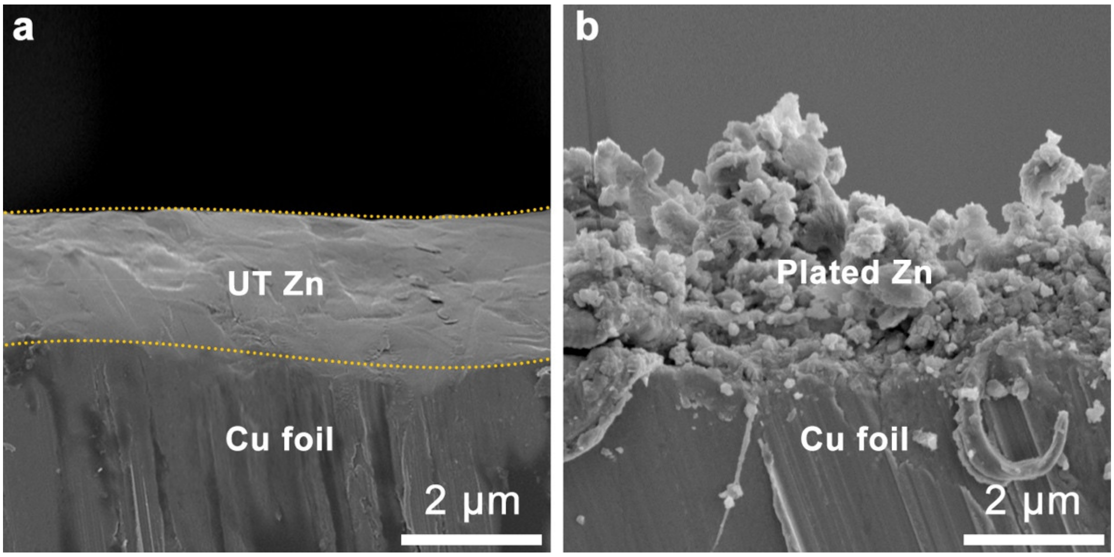

Figure S39. Cross-sectional SEM images of pristine UT Zn anode (a) before and (b) after 200 cycles in the MnO_2||Zn cell.

The thickness of the Zn layer is approximately 2.8 μm, characterized by a smooth morphology, as highlighted in the region between the yellow dotted lines in Figure S36a. After approximately 200 cycles in the full cell, the massive irregular products, which may come from the by-products and uneven Zn^{2+} plating, accumulated on the surface of the current collector as shown in Figure S36b. This indicates an irreversible Zn plating/stripping process and accumulation of by-products, likely due to the high Zn utilization of 91.5%.

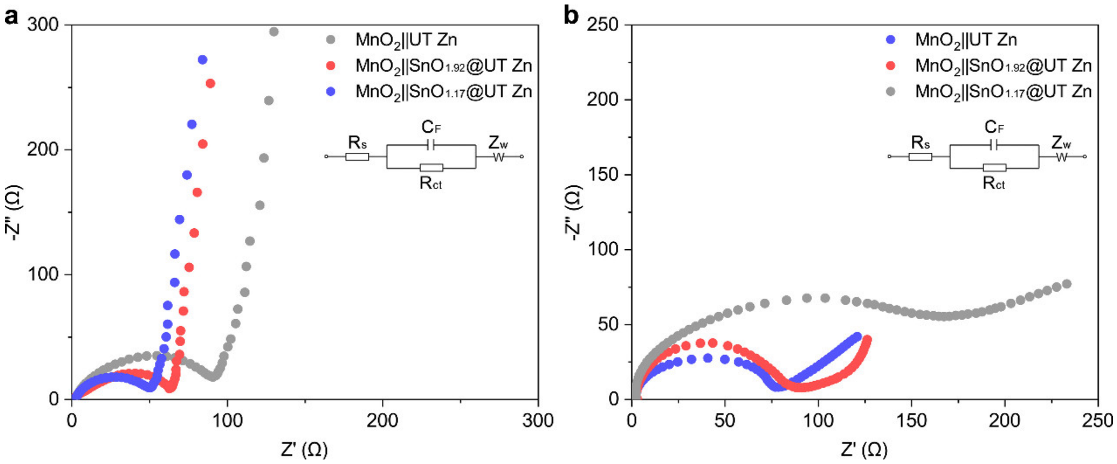

Figure S40. EIS spectra of the MnO_2||UT Zn, MnO_2||$SnO_{1.92}$@UT Zn, and MnO_2||$SnO_{1.17}$@UT Zn cells (a) before and (b) after 400 cycles under 0.1 A g^{-1}.

A large R_{ct} variation from ~94 Ω to ~183 Ω during 200 circulations can be observed in the MnO_2||UT Zn cell as demonstrated in Figure S37. The much lower R_{ct} changing from ~48 Ω to ~69 Ω and from ~57 Ω to ~87 Ω can be observed in the MnO_2||$SnO_{1.92}$@UT Zn and the MnO_2||$SnO_{1.17}$@UT Zn cells, respectively. This result implies the exceptional stability of the MnO_2||$SnO_{1.17}$@UT Zn cell compared to the other two samples.

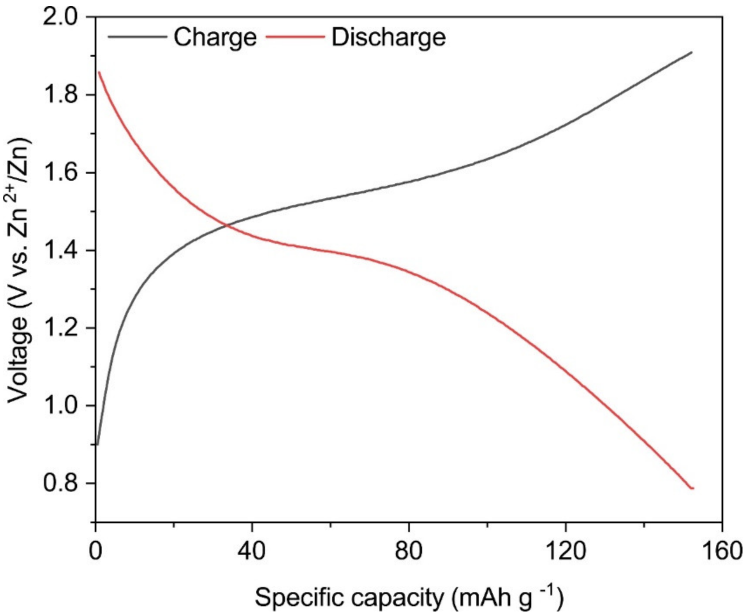

Figure S41. The charge-discharge profile of as-synthesized $ZnMn_2O_4$ cathode materials paired with pristine Zn metal anode under 0.05 A g^{-1}.

The $ZnMn_2O_4$ cathode delivered a specific capacity at around 155 mAh g^{-1} under 0.05 A g^{-1}, aligned with typical charge-discharge curves from previous reports.[25] The slopping plateau at the discharge curve represents the insertion/extraction of Zn^{2+} in the spinel structure of $ZnMn_2O_4$ cathode materials.[25b]

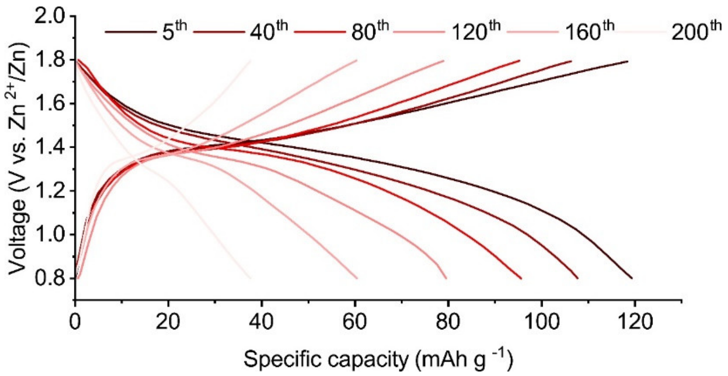

Figure S42. Selected charge-discharge profiles of $ZnMn_2O_4||SnO_{1.92}$@Cu cell at 0.1 A g^{-1}.

The charge-discharge curves of the $ZnMn_2O_4||SnO_{1.92}$@Cu cell at different cycles show a larger decrease in the discharge capacity during the cycling performance. In addition, the higher voltage decay of 0.09 V from 1.35 V at the 5th to 1.26 V at the 200th compared to the 0.03 V of $ZnMn_2O_4||$ $SnO_{1.17}$@Cu cell (from 1.39 at the 5th to the 1.36 at the 200th), suggest the more severe deteriorated electrochemical performance of the $ZnMn_2O_4||SnO_{1.92}$@Cu cell. Given that the same cathode was used in different cells, the observed differences in voltage decay primarily originate from the anode side which suggests that the $SnO_{1.17}$@Cu anode exhibits higher reversibility and more favorable kinetic conditions.

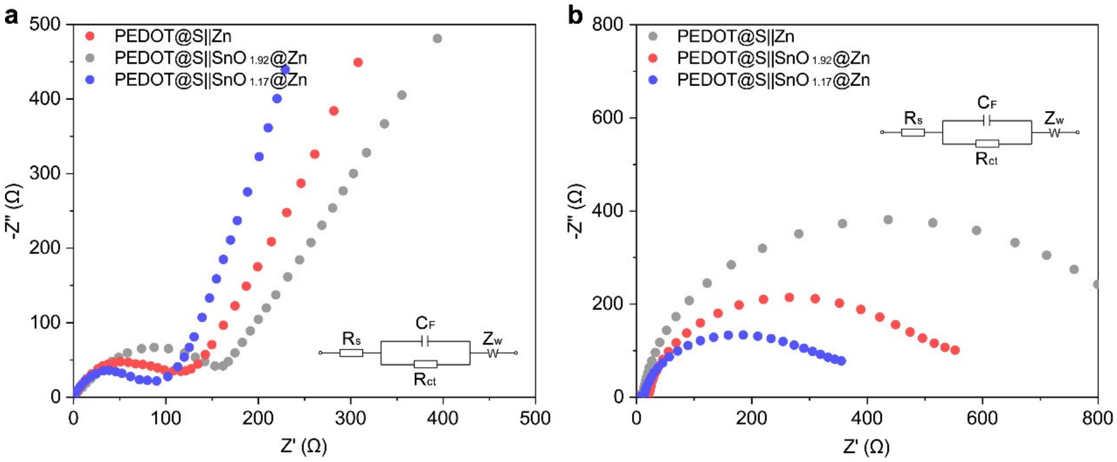

Figure S43. EIS spectra of the $ZnMn_2O_4$||Cu, $ZnMn_2O_4$||$SnO_{1.92}$@Cu, and $ZnMn_2O_4$||$SnO_{1.17}$@Cu cells (coin-type) at different cycles under 0.1 A g^{-1}.

The comparison of R_{ct} values between the $ZnMn_2O_4$||$SnO_{1.17}$@Cu cell (from ~63 Ω (before cycling) to ~75 Ω (200th cycle)) and $ZnMn_2O_4$||$SnO_{1.92}$@Cu cell (~83 Ω (before cycling) to ~104 Ω (200th cycle)) suggests the higher cycling stability of the $SnO_{1.17}$@Cu anode. In sharp contrast, the Rct of the $ZnMn_2O_4$||Cu cell significantly increased from ~125 Ω (before cycling) to ~230 Ω (47th cycle) during the cycling test, which may be attributed to the lack of a passivation (modification) layer on the Cu surface, resulting in the rapid degradation of the electrochemical performance.

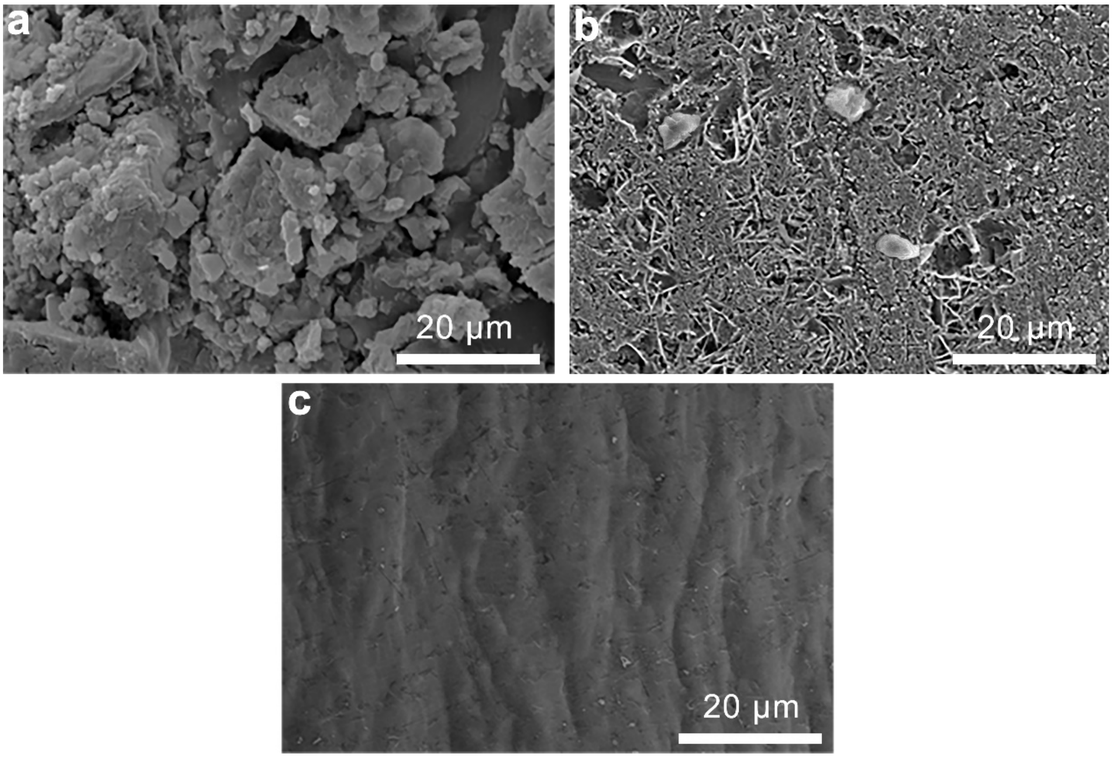

Figure S44. SEM images of cycled anodes in the anode-free (a) $ZnMn_2O_4$||Cu, (b) $ZnMn_2O_4$||$SnO_{1.92}$@Cu, and (c) $ZnMn_2O_4$||$SnO_{1.17}$@Cu cells.

As depicted in Figure S41a, the surface of the Cu substrate displays an uneven porous structure after 47 cycles in the full cell, revealing the significant corrosion reaction and the irreversible process of the Zn plating on the Cu substrate. On the surface of $SnO_{1.92}$@Cu substrate, the micro-sized particles and cavities can be observed in Figure S41b, which suggests the inevitable accumulation of by-products . In contrast, the smooth and uniform surface of the $SnO_{1.17}$@Cu anode in Figure S41c represents a highly stabilized electrode, suggesting the stabilized Zn^{2+} stripping/plating process in cell cycling.

Author Contributions

Y. Z. and S. L. conceived the idea, designed the experiments, wrote and revised the manuscript. Y. Z., M. K., F. Q., and D. H. L. performed experiments and formal analysis. C. S. K., J. P. and C. K. conducted related characterizations. F. L. helped with the analysis of the electrochemical data. S. L. supervised the project. H.-W. S. and S. L. provided the funding acquisition. And all the authors commented on the manuscript.

Supplementary References

[1] Y. Zhang, H. W. Song, K. R. Crompton, X. Yang, K. Zhao, S. Lee, *Nano Energy* **2023**, *115*, 108756.

[2] P. Giannozzi, S. Baroni, N. Bonini, M. Calandra, R. Car, C. Cavazzoni, D. Ceresoli, G. L. Chiarotti, M. Cococcioni, I. Dabo, A. Dal Corso, S. de Gironcoli, S. Fabris, G. Fratesi, R. Gebauer, U. Gerstmann, C. Gougoussis, A. Kokalj, M. Lazzeri, L. Martin-Samos, N. Marzari, F. Mauri, R. Mazzarello, S. Paolini, A. Pasquarello, L. Paulatto, C. Sbraccia, S. Scandolo, G. Sclauzero, A. P. Seitsonen, A. Smogunov, P. Umari, R. M. Wentzcovitch, *Journal of Physics: Condensed Matter* **2009**, *21*, 395502.

[3] J. P. Perdew, K. Burke, M. Ernzerhof, *Physical Review Letters* **1996**, *77*, 3865-3868.

[4] Z. Zhao, R. Wang, C. Peng, W. Chen, T. Wu, B. Hu, W. Weng, Y. Yao, J. Zeng, Z. Chen, P. Liu, Y. Liu, G. Li, J. Guo, H. Lu, Z. Guo, *Nature Communications* **2021**, *12*, 6606.

[5] P. E. Blöchl, *Physical Review B* **1994**, *50*, 17953-17979.

[6] J. Evans, C. A. Vincent, P. G. Bruce, *Polymer* **1987**, *28*, 2324-2328.

[7] Q. Deng, S. You, W. Min, Y. Xu, W. Lin, J. Lu, C. Yang, *Advanced Materials* **2024**, *36*, 2312924.

[8] T. Li, S. Hu, C. Wang, D. Wang, M. Xu, C. Chang, X. Xu, C. Han, *Angewandte Chemie International Edition* **2023**, *62*, e202314883.

[9] X. Huo, L. Xu, K. Xie, K. Zhang, J. Li, D. Wang, K. Shu, *Advanced Energy Materials* **2023**, *13*, 2203066.

[10] Y. Gao, N. Yang, F. Bu, Q. Cao, J. Pu, Y. Wang, T. Meng, J. Chen, W. Zhao, C. Guan, *Energy & Environmental Science* **2024**, *17*, 1894-1903.

[11] G. Li, Z. Zhao, S. Zhang, L. Sun, M. Li, J. A. Yuwono, J. Mao, J. Hao, J. Vongsvivut, L. Xing, C.-X. Zhao, Z. Guo, *Nature Communications* **2023**, *14*, 6526.

[12] X. Yang, Z. Zhang, M. Wu, Z.-P. Guo, Z.-J. Zheng, *Advanced Materials* **2023**, *35*, 2303550.

[13] A. Chen, C. Zhao, J. Gao, Z. Guo, X. Lu, J. Zhang, Z. Liu, M. Wang, N. Liu, L. Fan, Y. Zhang, N. Zhang, *Energy & Environmental Science* **2023**, *16*, 275-284.

[14] Y. Zeng, Z. Pei, Y. Guo, D. Luan, X. Gu, X. W. Lou, *Angewandte Chemie International Edition* **2023**, *62*, e202312145.

[15] X. Cai, X. Wang, Z. Bie, Z. Jiao, Y. Li, W. Yan, H. J. Fan, W. Song, *Advanced Materials* **2024**, *36*, 2306734.

[16] D. Feng, Y. Jiao, P. Wu, *Angewandte Chemie International Edition* **2023**, *62*, e202314456.

[17] K. Zhou, Z. Li, X. Qiu, Z. Yu, Y. Wang, *Angewandte Chemie International Edition* **2023**, *62*, e202309594.

[18] K. Ouyang, S. Chen, W. Ling, M. Cui, Q. Ma, K. Zhang, P. Zhang, Y. Huang,

Angewandte Chemie International Edition **2023**, *62*, e202311988.

[19] Z. Hu, F. Zhang, A. Zhou, X. Hu, Q. Yan, Y. Liu, F. Arshad, Z. Li, R. Chen, F. Wu, L. Li, *Nano-Micro Letters* **2023**, *15*, 171.

[20] Y. Chu, S. Zhang, S. Wu, Z. Hu, G. Cui, J. Luo, *Energy & Environmental Science* **2021**, *14*, 3609-3620.

[21] M. N. Islam, M. O. Hakim, *Journal of Materials Science Letters* **1986**, *5*, 63-65.

[22] aZ. Shen, J. Mao, G. Yu, W. Zhang, S. Mao, W. Zhong, H. Cheng, J. Guo, J. Zhang, Y. Lu, *Angewandte Chemie International Edition* **2023**, *62*, e202218452; bC. Yan, H.-R. Li, X. Chen, X.-Q. Zhang, X.-B. Cheng, R. Xu, J.-Q. Huang, Q. Zhang, *Journal of the American Chemical Society* **2019**, *141*, 9422-9429.

[23] X. Cai, H. Li, J. Li, H. Yan, Y. Liu, H. Yu, L. Yan, L. Zhang, J. Shu, *Ionics* **2021**, *27*, 3943-3950.

[24] aT. Shao, Y. Zhang, T. Cao, Y. Yang, Z. Li, H. Liu, Y. Wang, YongyaoXia, *Chemical Engineering Journal* **2022**, *431*, 133735; bN. Zhang, F. Cheng, Y. Liu, Q. Zhao, K. Lei, C. Chen, X. Liu, J. Chen, *Journal of the American Chemical Society* **2016**, *138*, 12894-12901.